



HAL
open science

Quantification of Crystalline Phases in Hf 0.5 Zr 0.5 O 2 Thin Films through Complementary Infrared Spectroscopy and Ab Initio Supercell Simulations

Rebecca Cervasio, Emilie Amzallag, Marine Verseils, Pierre Hemme, Jean-Blaise Brubach, Ingrid Cañero Infante, Greta Segantini, Pedro Rojo Romeo, Alessandro Coati, Alina Vlad, et al.

► To cite this version:

Rebecca Cervasio, Emilie Amzallag, Marine Verseils, Pierre Hemme, Jean-Blaise Brubach, et al.. Quantification of Crystalline Phases in Hf 0.5 Zr 0.5 O 2 Thin Films through Complementary Infrared Spectroscopy and Ab Initio Supercell Simulations. ACS Applied Materials & Interfaces, 2024, 16 (3), pp.3829-3840. 10.1021/acsami.3c13848 . hal-04771538

HAL Id: hal-04771538

<https://hal.science/hal-04771538v1>

Submitted on 7 Nov 2024

HAL is a multi-disciplinary open access archive for the deposit and dissemination of scientific research documents, whether they are published or not. The documents may come from teaching and research institutions in France or abroad, or from public or private research centers.

L'archive ouverte pluridisciplinaire **HAL**, est destinée au dépôt et à la diffusion de documents scientifiques de niveau recherche, publiés ou non, émanant des établissements d'enseignement et de recherche français ou étrangers, des laboratoires publics ou privés.

Quantification of crystalline phases in $\text{Hf}_{0.5}\text{Zr}_{0.5}\text{O}_2$ thin films through complementary infrared spectroscopy and *ab initio* supercell simulations

Rebecca Cervasio¹, Marine Verseils¹, Pierre Hemme¹, Jean-Blaise Brubach¹, Ingrid Cañero Infante², Greta Segantini³, Pedro Rojo Romeo³, Alessandro Coati¹, Alina Vlad¹, Andrea Resta¹, Yves Garreau¹, Claudia Decorse⁴, Bertrand Vilquin³, Emilie Amzallag⁴, Jérôme Creuze⁴✉, and Pascale Roy¹✉

¹Synchrotron SOLEIL, LOrme des Merisiers, Saint-Aubin BP 48, 91192 Gif-sur-Yvette Cedex, France

²Institut des Nanotechnologies de Lyon, CNRS UMR5270 ECL INSA UCBL CPE, 69621 Villeurbanne Cedex, France

³Université de Lyon, Institut des Nanotechnologies de Lyon (UMR5270/CNRS), Ecole Centrale de Lyon, 36 avenue Guy de Collongue, F-69134 Ecully Cedex, France

⁴ICMMO/SP2M, UMR 8182, Université Paris-Saclay, bat. 670 avenue des sciences, Orsay-F 91400, France

✉e-mail: jerome.creuze@universite-paris-saclay.fr; pascale.roy@synchrotron-soleil.fr

ABSTRACT

In the quest for thinner and more efficient ferroelectric devices, $\text{Hf}_{0.5}\text{Zr}_{0.5}\text{O}_2$ (HZO) has emerged as a potential ultra-thin and lead-free ferroelectric material. Indeed, when deposited on a TiN electrode, 1-25 nm thick HZO exhibits excellent ferroelectricity capability allowing the prospective miniaturization of capacitors and transistor devices. To investigate the origin of ferroelectricity in HZO thin films, we conducted a far-infrared (FIR) spectroscopic study on 5 HZO films with thicknesses ranging from 10 to 52 nm, both within and out of the ferroelectric thickness range where ferroelectric properties are observed. Based on X-ray diffraction, these HZO films are estimated to contain various proportions of monoclinic (m-), tetragonal (t-) and polar orthorhombic (polar o-) phases, while only the 11, 17 and 21 nm thick are expected to include higher amount of polar o-phase. We coupled the HZO infrared measurements with DFT simulations for these m-, t- and polar o- crystallographic structures. The approach used was based on the *supercell method*, which combines all possible Hf/Zr mixed atomic sites in the solid solution. The excellent agreement between measured and simulated spectra allows assigning most bands and provides infrared signatures for the various HZO structures including the polar orthorhombic form. Beyond pure assignment of bands, the DFT IR spectra averaging using a mix of different compositions (e.g. 70% polar o-phase + 30% m-phase) of HZO DFT crystal phases allows quantification of the percentage of different structures inside the different HZO films thicknesses. Regarding the experimental data analysis, we used the spectroscopic data to perform a Kramers-Kronig constrained variational fit to extract the optical functions of the films using a Drude-Lorentz based model. We found that the ferroelectric films could be described using a set of about 7 oscillators, which results in static dielectric constants in good agreement with theoretical values and previously reported ones for HfO_2 -doped ferroelectric films.

Key points: HfZrO_2 , Ferroelectricity, Thin films, Functional metal oxides, Infrared spectroscopy

Introduction

Ferroelectrics are a class of materials capable of two stable polarization states that need sufficient activation energy to pass from one to the other. These stable binary states are ideal for storing information of "0" and "1" kind in a nonvolatile manner. The activating energy to switch polarization implies an electric field, so these materials should have very low energy dissipation for applications such as different types of fast memory devices¹. As compared to the well-known perovskite ferroelectrics, fluorite-structure binary oxides are compounds with chemical formula MO_2 , with O^{2-} occupying the eight interstitial sites and M^{+4} ions occupy the regular sites of a face-centered cubic structure. These oxides have attracted considerable interest not only because they enable low-temperature synthesis but also for their Si-compatibility and scalability², as ferroelectricity has been verified in films of thickness down to 2.5³ and 1 nm². Moreover, avoiding lead in applications will be mandatory with new regulations.

The parent compounds ZrO_2 and HfO_2 have been intensively characterized in multiple physical forms, such as bulk, under high pressure, as thin films deposited on different substrates, nanocrystals and devices for over a century. Zr is the most

chemically similar element to Hf, therefore HfO₂ and ZrO₂ are usually called twin oxides because of their similar crystal structure⁴. Despite their large atomic number difference, 72 for Hf and 40 for Zr, their ions show very close ionic radii of 0.78 Å (Hf⁺⁴) and 0.79 Å (Zr⁺⁴)⁴. Regarding the phase diagram for both ZrO₂ and HfO₂, the monoclinic P2₁/c (m-phase, space group 14) is the most stable phase at room temperature and atmospheric pressure (see Fig. 1a). With the increase of temperature, a phase transition to the tetragonal P4₂/nmc structure (t-phase, 137) occurs at about 1700°C (1973 K) for hafnia and 1170°C (1443 K) for zirconia. Reaching even higher temperatures, one observes a transition to the cubic phase Fm3m (c-phase, 225) at about 2600°C (2873 K) for hafnia and 2370°C (2643 K) for zirconia (Fig. 1a). A different scenario is observed under hydrostatic compressive pressure: the m-phase passes to Pca2₁ (polar o-phase) and the two non-polar orthorhombics Pbca and Pnma.

Concerning the ferroelectric properties, the polar distortion is caused by the central anion displacement with respect to its surrounding cation tetrahedron, whereas in the non-polar tetragonal phase, the oxygen atom lies in the polyhedral centre of the tetrahedron. The evolution of the m-phase towards the high-symmetry t-phase and polar o-phase are favored by size effects, surface energies and confinement strains, that help on stabilizing inversion asymmetry².

HfO₂-doped films have a longer retention time, implying two stable binary polar states, than conventional ferroelectric perovskite materials. Theoretical work suggest that this higher retention could arise from the low static dielectric constant ϵ_s of about 17-25⁵. Devices containing materials with lower ϵ_s values in this range have less fringing fields, implying a uniform field near the edge of the plate capacitor. As a consequence, the significantly lowered dielectric constant of the polar o-phase HfO₂ may limit the retention loss, a problem arising from non-uniform field, especially in comparison with the perovskites counterparts⁶. Furthermore, this low- to mid- range ϵ_s allows polar switching at lower voltage compared to perovskite ferroelectrics⁷. The dielectric constant can be further used as a marker to identify a specific crystal structure, as the value of ϵ_s varies drastically for different HfO₂ phases: 29 for the cubic, 16 for the monoclinic, reaching its highest value for the t-phase (70)⁸. Notice however that there is a downside for the retention gain coming from the lower dielectric constant: as the ϵ_s lowers, the polarisation properties weaken as well.

Further information provided by the phonon behaviour has been reported by Delodovici et al.⁹ using first-principles simulations. The authors find that it is a strong trilinear coupling between three phonon modes that gives rise to the ferroelectric transition in HfO₂ doped materials, implying the stabilisation of the polar o-phase. Of the 3 phonons, one is only weakly unstable, whereas the other two are hard modes. This coupling between phonon modes leads to a polar distortion of oxygen atoms bonds along the *c* axis resulting in a spontaneous ferroelectric polarization parallel to this direction.

Since the first report of ferroelectricity in hafnium dioxide thin films¹⁰, many dopants were tested in order to further stabilize the polar o-phase. The family of promising dopants includes Zr, Y, Al, Gd, Sr, and La-HfO₂ based materials, with remnant polarization of 5 - 40 $\mu\text{C}/\text{cm}^2$ and coercive field of 0.75 - 4 MV/cm¹¹. To be able to stabilize the Pca2₁ polar o-phase, one needs to enhance the metal-oxygen bonding, which was achieved with the formation of a solid solution of ferroelectric compounds: Hf_{1-x}Zr_xO₂ for 0.3 < *x* < 0.5, *x* = 0.5 having the higher ferroelectric properties. Indeed, for HfZrO₂ films below ~ 30 nm, the ferroelectric polar o-phase is stabilized by a size-driven t- to polar o-phase transition. Besides that, the m- to t-phase transition temperature is significantly lowered when compared to ZrO₂ and HfO₂ bulk ones, leading to partially tetragonal (coming from ZrO₂) and partially monoclinic (coming from HfO₂) films¹².

The IR and Raman spectra of HfO₂, ZrO₂ and HZO have been studied in the literature using experiments and simulations, but only the parent compounds were investigated for all phases. Recent infrared reflectance measurements on Y-doped HfO₂ polar o-phase coupled with DFT phonon calculations have shown that the remnant polarization value in such bulk crystals is smaller compared with the reported value in thin film form¹³. This result is in accordance with the general idea that strain plays an extremely important role in these ferroelectric materials. In addition to experimental IR measurements on parent compounds, Materlik et al.⁷ have carried out DFT simulations to predict the IR spectra on multiple ZrO₂ and HfO₂ phases and on the polar o-phase for HZO, together with their static dielectric constants. This work revealed that transformation from the t-phase to the polar o-phase involves a small volume change from 131.8 Å³ to 133.8 Å³ while the polarization, in the *c* direction, does not change significantly. As a consequence, the transformation to the polar o-phase might come from a previous stabilized t-phase, even though both polar o- and t-phase have no close symmetry relationship. Although their work has widely contributed to the comprehension of the origin of ferroelectricity in such materials, experimental data on HZO are still lacking and a more complete representation of the large variety of the cells in HZO solid solution is needed. Indeed, the randomness of the HZO material can be reproduced by the use of a supercell model.

In this study, we coupled new HZO IR measurements with new DFT simulations for m-, t- and polar o- crystallographic structures (Fig. 1a). The simulation approach used a supercell method, chosen here as a two-unit cells for polar o- and m-, and four-unit cells for t-phase. This approach is validated by the spectroscopic study on 5 HZO films with thicknesses ranging from 10 to 52 nm both within and out of the thickness range where ferroelectricity is stabilized.

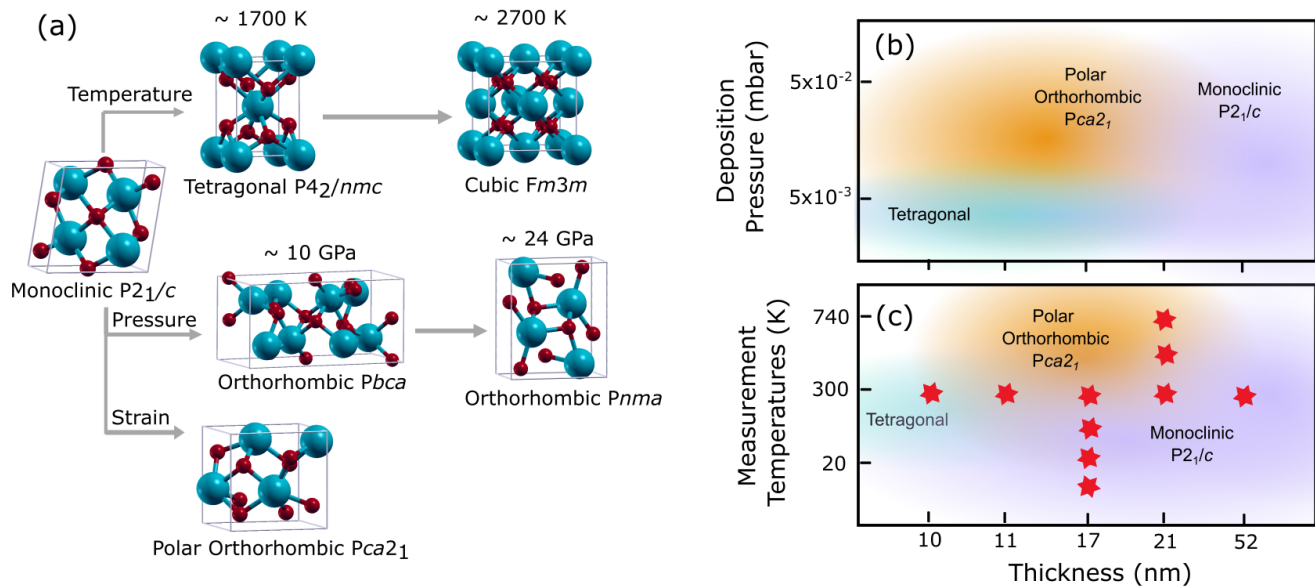


Figure 1. | Crystal structures of HZO samples (a) Different achievable space groups for HfO_2 and ZrO_2 bulk compounds. Blue spheres represents Zr or Hf, and O is in red. The ground stable m-phase transits to t-phase and further c-phase as temperature increases. A different path is observed for the increase of hydrostatic pressure: the m-phase transits to o-phase $Pbca$ and then to another o-phase space group, $Pnma$. If strain and thickness confinement are present, the polar o-phase $Pca2_1$ is observed. In addition, suggested schematic representation of HZO thin film phases for (b) two different deposition pressures and (c) different measuring conditions (temperatures and thickness) are presented. In (b), for the low argon pressure (5×10^{-3} mbar), HZO is dielectric (t-phase, blue zone). The HZO sample fabricated using this procedure has 10 nm thickness (HZO10). At higher argon pressure (5×10^{-2} mbar), HZO is ferroelectric, consisting of a mix of m- and polar o-phases. The samples (HZO11-52) deposited at this pressure have 11, 17, 21 and 52 nm thickness respectively. The thicker the films, the more the m-phase (purple zone) is present. After the deposition procedure, all samples go through a rapid thermal annealing at 450°C during 30 seconds under nitrogen atmosphere. Note that the thickness horizontal axis is not at scale. In (c), measured temperatures (red stars) and stable crystal phases (colored zones) are reported. At high temperatures, the polar o-phase (orange zone) is favored, whereas at low- T the m-phase (purple zone) is favored for samples fabricated using high argon pressure.

Experimental Results

The properties of optimally doped $\text{Hf}_{0.5}\text{Zr}_{0.5}\text{O}_2$ films with thicknesses of 10, 11, 17, 21, and 52 nm, designated here as HZO10, HZO11, HZO17, HZO21 and HZO52 were investigated. These films were grown on a $300 \mu\text{m}$ intrinsic IR transparent Si (001) substrate through magnetron sputtering with a single target (see *Methods - Sample Preparation*). The 10 nm sample was fabricated using a low-pressure method aiming at inducing the tetragonal phase, whereas the other samples were prepared using higher pressure, giving rise to a mix of m- and polar o-phases (Fig. 1b). The phase diagram of $\text{Hf}_{0.5}\text{Zr}_{0.5}\text{O}_2$ films formation is represented in Fig. 1b, in which the deposition pressure is plotted as a function of film thickness. Concerning the infrared measurements, the different probed temperatures are summarized in Fig. 1c and indicated by red stars, together with colored zones corresponding to the probed crystal phases. Prior to optical measurements, ferroelectricity was verified in the 11, 17 and 21 nm HZO samples by carrying P-E loop measurements using TiN (5 nm) as top electrode and doped Si substrate as bottom electrode (see P-E loop in Fig. S1 in the SI). The optical response of the intrinsic Si substrate measured in the same FIR absorption conditions were used as reference for calculating the absorbance (as illustrated in Fig. 2a). The room temperature measured absorbance for multiple thicknesses are shown in Fig. 2b. A series of strong transverse optical (TO) phonon modes is observed for all films. Starting from lower frequencies, when comparing to the standard HfO_2 modes, the phonon modes for all thicknesses, presented in Table 2, can be broadly identified as (frequencies are approximated): A_1 at 100 cm^{-1} , A_1 at 150 cm^{-1} , B_1 at 250 cm^{-1} , A_1 at 330 cm^{-1} , B_1 at 400 cm^{-1} , B_2 at 500 cm^{-1} and finally a A_1 mode at 600 cm^{-1} . In the following *Discussion* section, the main modes of each film are described in Tables 1 and 2. The evolution of the room temperature spectra as thickness increases involves the splitting of the 247 cm^{-1} band (HZO11) into 234 and 257 cm^{-1} (HZO17-52), together with the appearance of a small shoulder band at 304 cm^{-1} (HZO52), and a broadening and red shifting of the band at around 500 cm^{-1} . Finally, for the thickest film (HZO52), various high frequency structures develop around 570 to 680 cm^{-1} . Furthermore, for the thickest film, Fabry-Perot oscillations are observed.

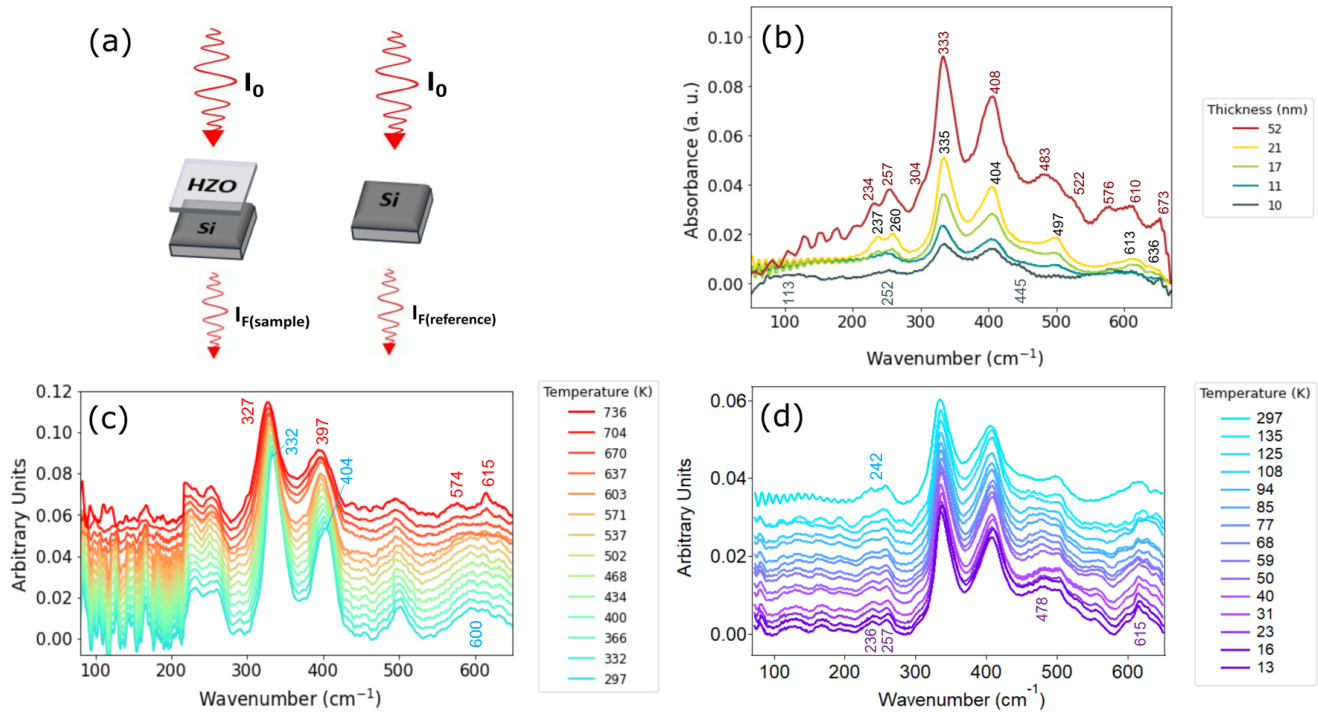


Figure 2. IR absorption spectroscopy (a) Schematic representation of absorption measurements method of HZO thin films deposited on intrinsic Si (001) substrate: thin film signal $I_{F(\text{sample})}$ (left) and reference signal $I_{F(\text{reference})}$ (right) are measured in the same experimental conditions. The IR absorbance (A) spectra is obtained by calculating $A = -\log(I_{F(\text{reference})}/I_{F(\text{sample})})$. (b) Room-temperature IR absorbance for different HZO thickness: 10 nm (mix t-/m-phase); 11, 17 and 21 nm (mix polar o-/m-phase) and 52 nm (m-phase). The spectra are plotted as measured with no shift on the absorbance of the curves. (c) Measured absorbance at high-temperatures of 21 nm ferroelectric HZO. (d) Measured absorbance at low-temperatures of 17 nm ferroelectric HZO. Spectra in (c) and (d) were shifted in absorbance for clarity, therefore represented in arbitrary units.

Temperature (T)-dependent FIR measurements were also conducted. The FIR absorbance results for HZO21 film, determined from 297 K to 736 K, are shown in Fig. 2c. As temperature increases, the band at 600 cm^{-1} splits into two small bands at 574 and 615 cm^{-1} . A softening of the two main bands at 332 and 404 cm^{-1} is also observed, shifting down to 327 and 397 cm^{-1} . Low-temperature (13 to 297 K) measurements are reported in Fig. 2d for HZO17. One can observe the splitting of the 242 cm^{-1} band (present at $T = 297\text{ K}$) into 236 and 257 cm^{-1} as T decreases. In addition, a new band gradually appears at 478 cm^{-1} at low temperatures, together with the narrowing of the 615 cm^{-1} band. These limited modifications confirm the stability of the structures.

The grazing incidence X-ray diffraction (GIXRD) experiments were carried out at the UHV end-station of the SixS beamline at Synchrotron SOLEIL. Measurements were carried out at room temperature on two samples (HZO11 and HZO21) (see Fig. S2 in the SI for more details).

Density Functional Theory Results

Ab initio calculations were carried using the 2017 version of the CRYSTAL code¹⁴, based on a linear combination of atomic orbitals method for the crystalline orbitals expansion. Using the PW1PW functional, IR spectra composed of TO modes, convoluted at a bandwidth of 30 cm^{-1} were simulated (more details on the simulations are found in the *Computational section* in *Methods*).

DFT Results for ZrO_2 and HfO_2

To assess the three HZO phases of interest, m-, t- and polar o-phases, we firstly simulated the IR spectra of the parent compounds ZrO_2 and HfO_2 (Fig. 3). Not only this allows us to validate the simulation parameters, but the comparison between parent compounds and HZO provides a first assignment of each band vibration. Moreover, our results are in very good agreement with previous theoretical work carried by El Boutaybi et al. for m-, t- and o- phases of zirconia¹⁵ and Materlik et al.⁷.

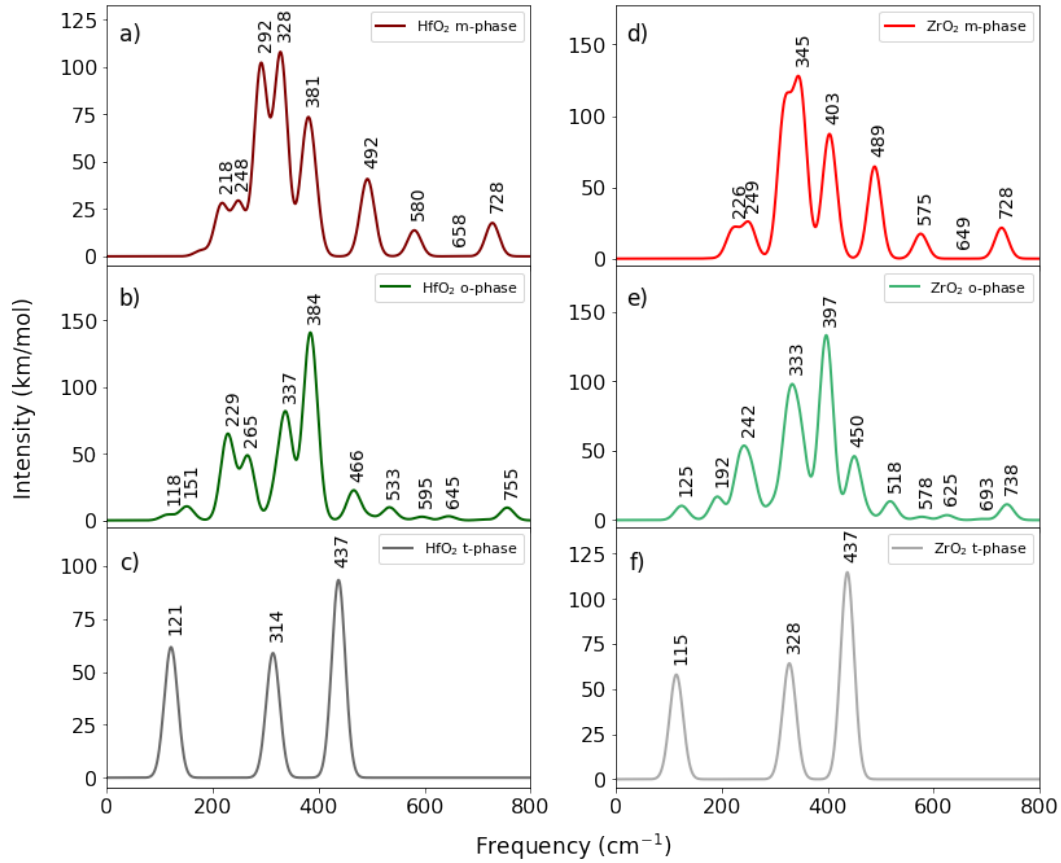


Figure 3. | DFT far-infrared spectra of parent compounds HfO_2 and ZrO_2 . In (a, b, c) the DFT spectra of HfO_2 is presented and in (d, e, f) for ZrO_2 . The m-phase (top panel, red), o-phase (middle panel, green) and t-phase (bottom panel, gray) are reported.

DFT Results for HfZrO_2 - Supercell Method

To take into account the complexity of a real solid solution system, the supercell approach is used. It consists in generating all possible combinatorial HZO configurations of Zr/Hf mixed atomic sites (blue spheres in Fig. 1) in the composition 50% Zr - 50% Hf. To be constant in the total number of atoms (24), the method implies the use of four unit cells for the t-phase ($1 \times 2 \times 2$, $2 \times 1 \times 2$, $2 \times 2 \times 1$) and two unit cells for m- and polar o-phases ($1 \times 1 \times 2$, $1 \times 2 \times 1$, $2 \times 1 \times 1$) in the three directions of space. The supercell approach has been presented before for a similar solid solution system in references^{16,17}. In the present paper, FIR spectra were simulated for HZO in its polar o-phase (space group 29, $Pca2_1$), for the t-phase (137, $P4_2/nmc$) and the most stable m-phase (14, $P2_1/c$). For the o-phase, two-unit cells ($1 \times 1 \times 2$, $1 \times 2 \times 1$, $2 \times 1 \times 1$) give rise to a series of 70 possible configurations, and thanks to the symmetric degeneracy present in the system^{18,19}, the number of configurations N decreases to 39 (12 for $1 \times 1 \times 2$, 14 for $1 \times 2 \times 1$ and 13 for the $2 \times 1 \times 1$ supercell). For the m-phase, 40 possible configurations exist, whereas for the t-phase, 26 different supercell configurations are found. The FIR spectrum for each configuration can be found in the SI (from Fig. S8 to S16). To thermodynamically evaluate the configuration's distribution, the weighted average for each supercell crystal structure (m-, polar o- and t-phases) of FIR spectra is presented in Fig. 4. These reported theoretical IR spectra, here called $\bar{I}_N(\nu, T)$, are obtained from the $I_i(\nu)$ IR spectra corresponding to each of the N configurations for the 3 different supercells for each phase¹⁶, following:

$$\bar{I}_N(\nu, T) = \sum_{i=1}^N P_i(V, T) \times I_i(\nu) \quad (1)$$

and by using the Boltzmann occupation probability, $P_i(V, T)$, given by²⁰:

Simulated TO Frequencies (cm ⁻¹)								
Tetragonal (137, P ₄₂ /mnc) energy = 89 meV			Orthorhombic (29, Pca ₂₁) energy = 52 meV			Monoclinic (14, P2 ₁ /c) energy = 0 meV		
Mode Symmetry	Simulation	Observed HZO10	Mode Symmetry	Simulation	Observed HZO21	Mode Symmetry	Simulation	Observed HZO52
E _u	116	~100	A ₁	136	160			
			B ₁	238	237	B _u	230	234
A _{2u}	325	335	B ₂	255	260	A _u	249	257
			A ₁	333	335	B _u	337	333
E _u	447	445	B ₁	397	404	A _u	405	408
			A ₁	460				
			B ₁	530	497	B _u	503	483
						A _u	594	576
			A ₁	597	613			
			B ₂	640	636			
			B ₁	748		B _u	738	673

Table 1. Theoretical TO frequencies together with their symmetries and comparison with observed values. The symmetry modes were taken from ZrO₂ simulations, owing to complexity of HZO analysis. Experimental frequencies were taken from the fit (for each corresponding thickness) and only the values that match the theoretical ones are present (see Table 2 for all experimental values). Although all samples present a mix of various phases, for simplicity, the t-phase simulation is compared with the 10 nm HZO sample (HZO10), the polar o-phase with the 21 nm (HZO21) and the m-phase with the 52 nm one (HZO52). In bold, the theoretical polar modes are highlighted, implying DFT modes with TO–LO shift > 200 cm⁻¹ (LO stands for longitudinal optical mode). Reported formation energies in meV are normalized to the lowest energy of the m-phase.

$$P_i(V, T) = \frac{m_i \exp\left(-\frac{E_i}{k_B T}\right)}{\Omega} \quad \text{with} \quad \Omega = \sum_{i=1}^N m_i \exp\left(-\frac{E_i}{k_B T}\right). \quad (2)$$

In Eq. 2, E_i is the total energy of the i^{th} configuration per chemical unit (1 Hf/Zr + 2 Oxygen atoms) at its optimized geometry with volume V , neglecting the zero-point energy, m_i is the multiplicity of the i^{th} configuration, T is the temperature in Kelvin and k_B is the Boltzmann's constant. The choice of T is done by analyzing the film's deposition process: sputtering at room-temperature (300 K) and further annealing at 723 K. As the desired phases are only obtained during annealing, the temperature chosen for averaging the spectra is $T = 723$ K.

Discussion of Results

Spectroscopic Measurements and Simulations

The assignment to either the m-phase P2₁/c, which is the most stable phase at room temperature, and the desired polar o-phase Pca₂₁ is challenging because both phases exhibit a plethora of far-infrared (FIR) bands. Moreover, the growing process can result in a mix of structures within the material. Room-temperature X-ray diffraction (XRD) measurements (see Fig. S2 of the SI) confirmed the mix of structures for films of 11 and 21 nm. The calculated diffractogram for the three phases of HZO are presented in the SI (Figure S2). The very large number of peaks and their look alike diffractogram make it hazardous to base

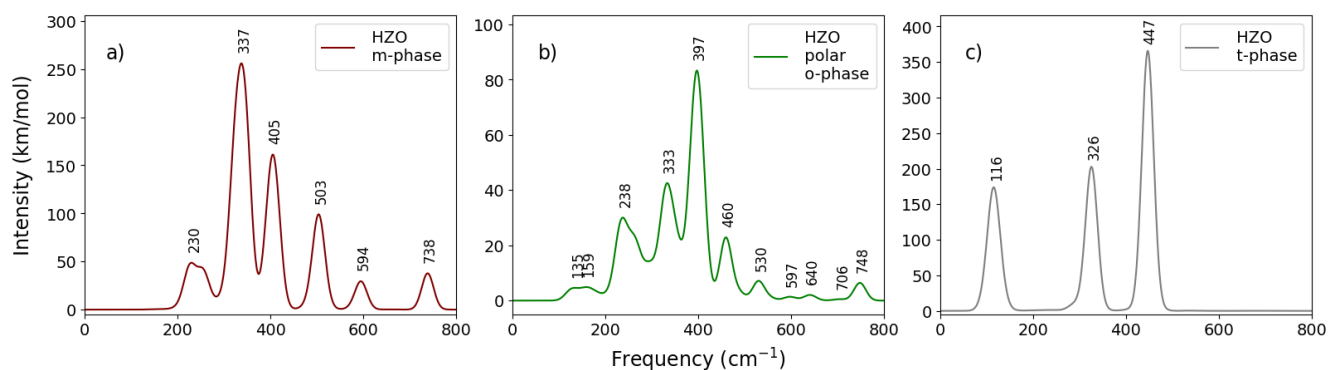


Figure 4. IDFT far-infrared weighted average spectra for the HZO supercells for the (a) stable m-phase (14, $P2_1/c$), (b) polar o-phase (space group 29, $Pca2_1$) (c) t-phase ($P4_2/nmc$). Inside each crystal structure family, the many configuration spectra are averaged using the degeneracy of each configuration, together with its Boltzmann probabilistic weight at $T = 723$ K.

the assignment of the thin films to one (or a combination of) crystallographic structure. However, one series of peaks between $2\theta = 12-14$ seems to vary significantly from one structure to the other (see insert of Fig. S2). Indeed, in this range, two peaks are calculated for the monoclinic phase, while the calculation for both orthorhombic and tetragonal ones leads only to one peak at an intermediate position around 23° . In contrast, in this 2θ range, the diffraction measurements on HZO11 shows three peaks while there are only two intense peaks for HZO21 and a tiny third peak in between them. This observation suggests that the HZO21 film contains more monoclinic than the HZO11 one, both being a mix of monoclinic with either orthorhombic or tetragonal phase. In the following, we will see that a comparison of the phonon structures observed for the various films grown under various conditions with the simulated infrared spectra for the various HZO phases allows not only a non-ambiguous identification of the phases present inside the samples, but also their quantification.

The analysis of the main IR bands obtained from DFT simulations can help identify the type of collective atomic vibration responsible for such bands. Table 1 summarizes the theoretical and experimental frequencies, as well as the mode symmetries, for the three main phases. It also reports the formation energies for each phase in meV, normalized to the energy of the m-phase. Regarding the type of vibration, the theoretical m-phase presents pure bending modes for the 230 and 249 cm^{-1} bands, whereas the other bands are a mix of both stretching and bending. In a similar fashion, the polar o-phase presents 136, 255 and 397 cm^{-1} bands as fully bending modes, and finally the t-phase presents only the 325 cm^{-1} as pure bending.

In light of these theoretical results, experimental far-infrared bands can be tentatively assigned to the m- and polar o-phases in ferroelectric samples: in Fig. 2, for thickness corresponding to dominant monoclinic, the experimental 247 cm^{-1} band characteristic of the polar o-phase (HZO11) splits into 234 and 257 cm^{-1} bands characteristic of the m-phase (HZO52). This is in accordance with similar bands in our DFT results in Fig. 4a-b for m-phase 14 and o-phase 29 (Table 1). Therefore, the A-symmetry modes at around 130 and 460 cm^{-1} and the B modes at 530 and 640 cm^{-1} can be used to identify the polar o-phase, as it is known for hafnia¹³. This is an important distinction when comparing it with the m-phase of similar IR signature.

Regarding the 10 nm sample, it has been fabricated using a low-pressure method (Fig. 1b), in which the t-phase is favoured relative the polar o- or m-phases. One can notice however, that its phonon profile seems globally similar to the m-phase, significantly differing from the simulated t-phase spectrum (see DFT section, Fig. 4c, t-phase 137). Nevertheless, the most striking feature is the large (~ 50 cm^{-1} width) band centered at about 100 cm^{-1} (refer to Fig. S3 and S4a for better visualisation). This band seems to be intrinsically related to the t-phase, as it is not present in any other thickness. Our DFT results in Fig. 4c show three very intense bands for this t-phase, implying 116, 325 and 447 cm^{-1} . We can therefore suggest that the very intense 100 cm^{-1} band present in the 10 nm sample corresponds to the 116 cm^{-1} band predicted by DFT. Other interesting remarks for the HZO10 spectrum in Fig. 2b are: (i) the experimental 252 cm^{-1} band is not doubled as expected for a sample containing in part the m-phase, and (ii) one observes a shoulder band around 445 cm^{-1} , in accordance to the expected DFT t-phase band at 447 cm^{-1} (Fig. 4c). We can therefore conclude that the 10 nm sample is a mix of t- and m-phases.

As mentioned earlier, the HZO films are a mix of two phases: tetra + m-phase for (HZO10) and polar ortho + m-phase for (HZO11-21). The quantification of such crystal phases mix that constitute the HZO films can be achieved by carrying a weighted average of the DFT spectra of different compositions of tetra + m-phase and polar ortho + m-phase. To determine the proportions of each phase, one can vary the averaging of two DFT FIR spectra from 0% of t-phase and 100% of m-phase, until 100% t-phase and 0% m-phase in steps of 10% (see examples in Fig. S6 and S7). To evaluate which composition (percentage of phases) is the closest to the experimental FIR spectra, one can then quantify the similarity between the spectra using an evaluation metric, using the well known coefficient of determination R^2 , as demonstrated in previous studies for the

Samples	Experimental IR Frequencies in cm^{-1} : ω_{TO} (ω_{LO})										
HZO52		234 (234)	257 (266)	304 (-)	333 (365)	408 (459)	483 (547)	522 (547)	576 (589)	610 (629)	673 (672)
HZO21		237 (~ 241)	260 (269)		335 (367)	404 (479)	497 (557)			613 (587)	636 (647)
HZO17	160 (177)	236 (~ 246)	259 (268)		334 (368)	404 (486)	496 (560)			612 (~ 620)	641 (785)
HZO11	149 (~ 170)		247 (270)		334 (368)	404 (486)	496 (534)	589 (589)		612 (624)	
HZO10	113 (~ 170)	194 (~ 218)	252 (271)		338 (373)	402 (529)	445 (~ 500)	495 (529)	581 (688)		700 (859)

Table 2. Experimental HZO IR frequencies for multiple film thickness (52, 21, 17, 11, 10 nm). The transversal mode frequencies ω_{TO} are taken as maxima of the corresponding absorbance spectra, whereas longitudinal mode frequencies ω_{LO} , inside parenthesis under ω_{TO} , are taken from the maxima of the dielectric loss function $-\text{Im}(1/\epsilon) = \epsilon_2/(\epsilon_1^2 + \epsilon_2^2)$ (Fig. S5) as this function describes the system response to the longitudinal displacement of atoms. HZO10 is a mix of t- and m- phases, HZO52 is m-phase and the others are a mix of m- and polar o- phase (ferroelectric). Similar frequencies are vertically aligned for clarity. HZO10 presents bands at 113 and 445 cm^{-1} attributed to the t-phase. Simulated frequencies can be found in Table 1.

extraction of quantitative information from IR data^{21,22}. By minimizing R^2 , one obtains the DFT mixed compositions closest to the experimental ones. To do so, both theoretical and experimental spectra were scaled to 1 using a scaling factor. Fig. 5 compares the experimental FIR spectra of HZO films with the mixed-phases' spectra with minimum R^2 . The comparison between HZO10 (Fig. 5a) and the different percentages of DFT mixed-phases yields the highest $R^2 = 0.4138$ for the 70% m-phase + 30% t-phase. For the ferroelectric samples HZO11, the highest R^2 was 90% (0.7133), for HZO17 70% (0.8281) and HZO21 60% (0.8858) of polar o-phase, plotted in Fig. 5e. The mostly m-phase HZO52 sample yields the highest R^2 of -0.5243 for 100% m-phase. The negative value of R^2 indicates lower correlation between experimental and theoretical data, most likely coming from the higher background in Fig. 5c. These results were verified using three error evaluations (*mean absolute error*, *mean squared error* and *root-mean squared error*) which yielded similar percentage trends. This analysis based on measured and theoretical IR data allows therefore a quantification of crystal phases in thin films, which is not possible with more standard X-ray diffraction measurements in the present case.

We now examine whether the modifications present in the temperature dependent measurements (Fig. 2c-d) help to clarify if a phase transition occurs in HZO thin films at high temperatures when compared to bulk HZO. At low temperatures (13 K to 297 K, Fig. 2d), the 17 nm HZO film presents the gradual increase in intensity of the 478 cm^{-1} band, possibly corresponding to the more stable monoclinic phase (see Fig. 4a for the DFT spectra of the m-phase). This measurement also helps to better correlate the DFT simulated phonon bands to the experimental ones, as the DFT calculation are carried out for an infinity structure at 0 K. At high temperatures (Fig. 2c), a slight softening of the main modes at 332 and 404 cm^{-1} is observed, together with the splitting of the 600 cm^{-1} band into 574 and 615 cm^{-1} . Although the first high-temperature phase in bulk HZO materials is the t-phase (at about 1700°C (1973 K) for hafnia and 1170°C (1443 K) for zirconia), the frequencies of the observed new bands (574 and 615 cm^{-1}) do not correspond to any predicted t-phase bands (Fig. 1c). Contrary to what is expected, this temperature effect is attributed to a possible reinforcement of the polar o-phase, as DFT simulations predict two bands at about 590 and 640 cm^{-1} (Fig. 4b). This is an important result, as it suggests that the heating of these very thin films does not causes the loss of ferroelectricity, as would be expected from its parents' phase diagram (transition to t-phase, Fig. 1a). This result may support the use of such films for technological applications in which the sample is heated up to high temperatures.

Extraction of Optical Functions

To extract the optical properties of HZO thin films, a Drude-Lorentz model can be used. By fitting a Kramers-Kronig constrained function process, one can obtain the complex optical parameters: complex dielectric function (ϵ_1 and ϵ_2), refractive indexes (n and k) and the conductivity function (σ_1 and σ_2). To achieve a good fit, one needs a broadband IR measurement. We therefore carried measurements from 15 to 5500 cm^{-1} . The input parameters are the film thickness, the angle of incidence (80°), the IR absorption data, together with a series of oscillators that act as a starting point for the fit algorithm. A Lorentz oscillator is described by its frequency (ω_0), its intensity (ω_{pl}^2) and scattering rate γ . In order to implement the Drude-Lorentz model,

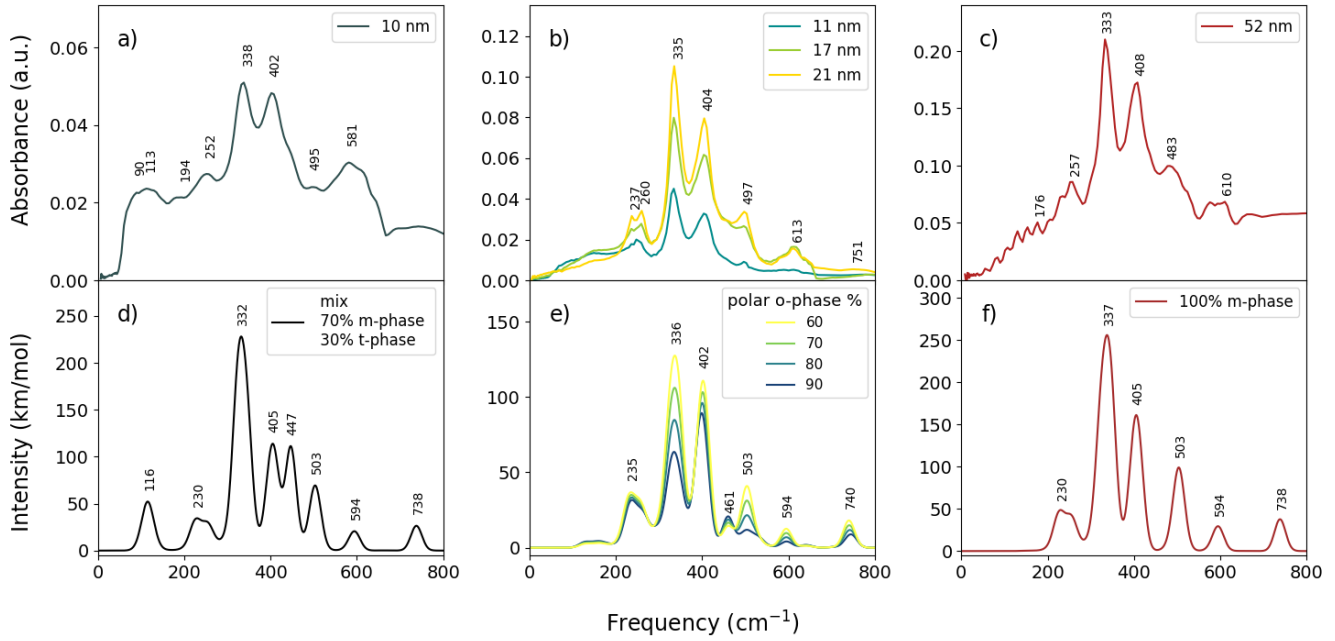


Figure 5. | Comparison between far-infrared (FIR) spectra of experimental HZO thin film measurements (a-c) and theoretical mixes (d-f) of different compositions of DFT supercell spectra for the HZO compound. Experimental FIR spectra are (a) HZO10 (b) HZO11, HZO17 and HZO21, (c) HZO52. The theoretical DFT FIR spectra mixes are (a) 70% t-phase ($P4_2/nmc$) + 30% m-phase, (b) from 60 to 90% polar o-phase (space group 29, $Pca2_1$) mixed with corresponding 40 to 10% m-phase, (c) 100% stable m-phase (14, $P2_1/c$).

REFFIT²³ software was exploited. The algorithm is implemented in what is called the "Variational Dielectric Function" (VDF) method²⁴. This VDF method, also referred as "free-shape" method, uses the Drude-Lorentz oscillator function to fit the data point-by-point, as any physical dielectric function can be approximated with very good accuracy by some set of Lorentzian oscillators²⁴. For ferroelectric HZO21, the starting point is a model based on 7 fixed oscillators, with frequency ω_0 based on the maxima of the absorbance spectra (see Table S1 in the SI for details), in accordance with the IR active oscillators of highest intensity predicted by the DFT calculations.

In Fig. 6a, we report the resulting VDF fit (orange) together with the broadband IR data for HZO21 (blue line). A good accuracy of the fit can be observed. Figures 6b-d report the optical functions extracted: the dielectric function (b), refractive index (c) and optical conductivity (d). Fig. 6b shows the real (ϵ_1 , blue line) and imaginary part (ϵ_2 , orange line) of the dielectric function for the HZO21 at room temperature (all fitting starting point parameters are reported in Table S1 of SI). From the real part of the dielectric function ϵ_1 in Fig. 6b, one can extract ϵ_s , the static dielectric constant ($\epsilon_s = \epsilon_1(\omega = 0)$). For sample HZO21, one obtains $\epsilon_s = 29$, in agreement with previous studies for doped-HfO₂^{7,11} and is in reasonable agreement with our DFT calculations results for the polar o-phase (22, Table 3).

To expand the ϵ_s analysis, Fig. 7a reports ϵ_1 for all thickness and phases. The high quality of the fit can be observed in Fig. 7b for all thicknesses. Table 3 presents the extracted ϵ_s for all samples, together with simulated and literature values. Interestingly, HZO17 (polar o-phase) sample reveals a ϵ_s value of 24 (see also Fig. S4 in the SI), a lower static dielectric constant than its polar o-phase counterparts HZO11 (27) and HZO21 (29). This lower ϵ_s may favor a lower retention time in devices, giving rise to better ferroelectric properties in thinner films. The most striking ϵ_s value is, however, the one associated to HZO10 (t-phase), reaching 56 in comparison with the maximum value of 29 (HZO21) for the polar o-phase samples, the theoretical ϵ_s value for the t-phase falling in the range 60-70⁸. Note that DFT simulated ϵ_s are second rank tensors represented by matrices¹⁴. Each supercell configuration generates one ϵ_s matrix. Using the weighted average taking the Boltzmann occupation probability, $P_i(V, T)$, we obtain the averaged ϵ_s matrix for one phase. To obtain a scalar ϵ_s value, the matrices were diagonalized and the average value for the diagonal was taken for the polar o-phase and m-phase. For the t-phase, however, the ϵ_s along the c direction (60) was taken as it was closer to the experimental value (56), indicating a possible preferential orientation of the film in this direction. A visual comparison between the extracted from fit and DFT calculated ϵ_s values is presented in Fig. 8.

The fit of the IR broadband data allows also inferring the longitudinal frequency modes (ω_{LO}) that are not directly measured

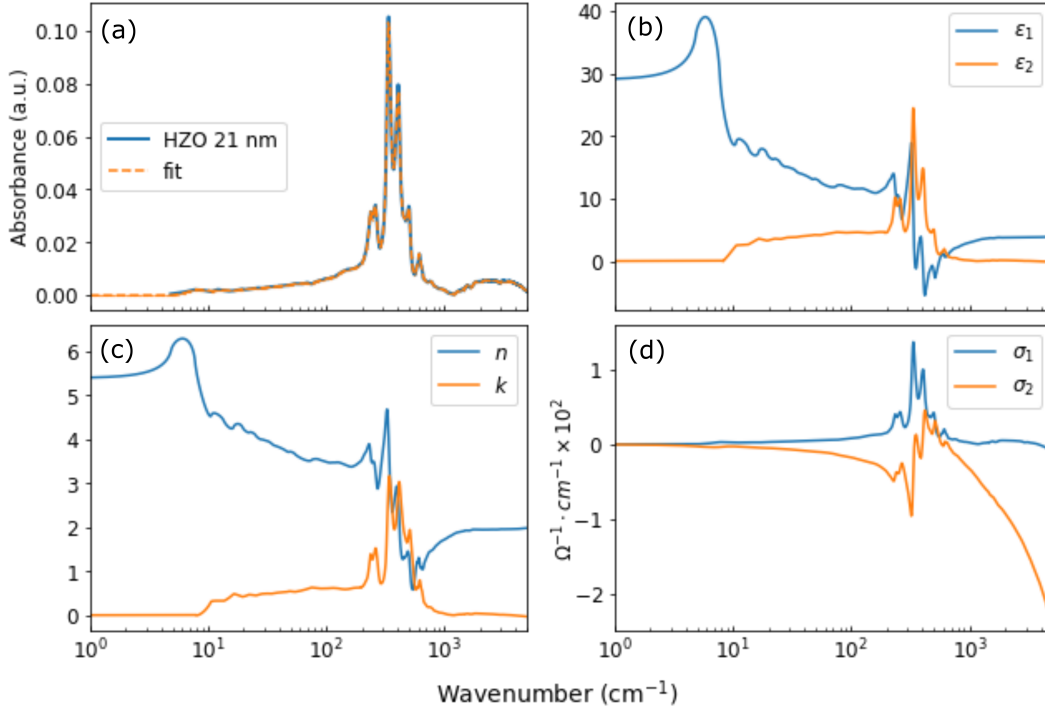


Figure 6. | Optical functions extracted using a Drude-Lorentz model (a) IR absorption data ($15\text{-}5500\text{ cm}^{-1}$) for the 21 nm HZO sample (blue) and fit (orange dotted line) (b) Real (blue) and imaginary (orange) parts of the dielectric function (c) Real (blue) and imaginary (orange) parts of the refractive index (d) Real (blue) and imaginary (orange) parts of the optical conductivity.

by absorption. ω_{LO} for many modes are taken from the maxima of the dielectric loss function $-\text{Im}(1/\epsilon) = \epsilon_2/(\epsilon_1^2 + \epsilon_2^2)$, and are summarized in Table 2. The dielectric loss functions are reported in Fig. S5 for all samples, together with the corresponding absorbance data. In our polar o-phase samples, the mode with the highest TO–LO splitting (84 cm^{-1}) is at 404 cm^{-1} , which is a B_1 symmetry mode with only bending characteristics.

In summary, the VDF method implemented in the REFFIT software allows a "free-shape" fitting of the absorption data, being particularly useful for thin films as one can easily input the sample thickness and angle of incidence. The fit allowed the extraction of different optical functions that characterize each materials' crystal phase, and ultimately the extraction of the static dielectric function ϵ_s and LO mode frequencies, which are parameters intrinsically related to ferroelectric properties.

Conclusion

We investigated multiple HZO film of thickness 10, 11, 17, 21 and 52 nm using IR spectroscopy and interpreted the spectra based on DFT calculations adapted to the study of solid solutions. Such interpretation remains ambiguous with X-ray diffraction method. To investigate the three main phases, we provided a complete IR spectroscopic overview of the HZO thin film materials, together with the extraction of optical properties (dielectric function, refractive index, optical conductivity, TO and LO modes) from broadband IR measurements. By comparison with supercell DFT calculations for t-, polar o- and m- phases, we observe characteristic FIR bands that can be used as signatures for identifying the ferroelectric phase in HZO thin films. This comparison confirms that the argon pressure during film deposition and its thickness have direct influence on the final crystal structure: t- and m- phases for HZO10, polar o- and m- phase for HZO11 to HZO21 and m-phase for HZO52, pointing out at the role played by the strain⁷. We also verify that the m-phase is the most stable and the polar o-phase is responsible for ferroelectricity in such films. Beyond that, the quantification of mixed phases inside HZO thin films is possible thanks to the averaging of t-/m-phase and polar o-/m-phase DFT spectra for multiple compositions. By taking advantage of the coefficient of determination R^2 , DFT spectra of mixed-phases are quantitatively compared to experimental ones, allowing quantification of the percentage of each phase inside the films. Concerning the temperature resolved measurements, the polar o-phase seems to be stable even at high-temperatures, an important result for some applications in which heating up the sample is needed. Therefore, IR spectroscopy coupling measurements and theoretical calculations emerges as an important tool to characterize

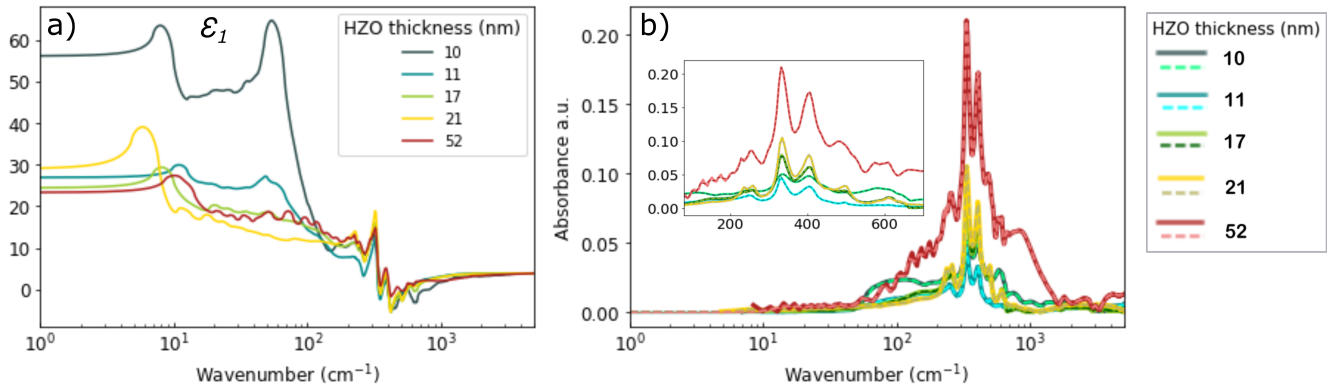


Figure 7. | Real part of the dielectric function ϵ_1 and IR absorbance data and fit for multiple thickness (a) The optical function ϵ_1 was obtained through a Kramers-Kronig constrained variational fitting carried for multiple film thickness: 10 nm (t-phase); 11, 17 and 21 (mix polar o-, m-phases); 52 nm (m-phase). (b) IR absorbance data (full-lines) and fit (dashed-lines) for the same films. Notice that both (a) and (b) plots are in logarithm scale. The inset in (b) shows a magnification on the far-infrared region (normal frequency scale).

ferroelectric materials, especially allowing the identification of signature polar bands.

Methods

Sample Preparation

Fabrication of HZO thin films is carried out using a magnetron sputtering deposition at room temperature (300 K). To induce the polar o-phase, high argon pressure was used (5×10^{-2} mbar) inside the sputtering system. To induce the t-phase, a lower argon pressure of 5×10^{-3} mbar is used. The deposition is followed by a rapid thermal annealing at 450 °C for 30 seconds under a nitrogen atmosphere.

Spectroscopic Measurements

The film optical properties were probed using the infrared spectroscopy beamline AILES (Advanced Infrared Line Exploited for Spectroscopy), Synchrotron SOLEIL²⁵. Exploiting the high brightness of the synchrotron radiation source. THz and FIR spectra in the 15 – 600 cm^{-1} range and MIR spectra (up to 5500 cm^{-1}) were obtained using a Bruker IFS125HR Fourier transform spectrometer evacuated at pressures lower than 10^{-4} mbar to avoid absorption by water and residual gas. The (15 – 60 cm^{-1}) spectral range was measured with a resolution of 0.5 cm^{-1} using a 50 microns Mylar beamsplitter combined with a bolometer cooled at 1.6 K, having a signal-to-noise ratio of 1700:1. For the (40 – 600 cm^{-1}) range, a spectral resolution of 2 cm^{-1} was chosen. A 6 microns Mylar beamsplitter combined with a bolometer cooled at 4.2 K complete the set-up. A low vibration pulse tube cryostat was used to achieve temperatures down to 13 K from room temperature. This system contains a sample holder which is mechanically decoupled from its cold finger, allowing minimum sample vibrations. High temperature measurement were performed using the T95 Linkam oven manually adapted to the spectrometer.

Computational section - Density Functional Theory Calculations

Ab initio calculations were carried out using the 2017 version of the CRYSTAL quantum solver¹⁴, which is based on a linear combination of atomic orbitals (LCAO) for the crystalline orbitals (CO) expansion. More precisely, CRYSTAL uses Gaussian-type functions (GTF) as atomic orbitals (AO) basis sets (BS). Here, we chose the common (popular among CRYSTAL users) pob-TZVP-rev2 basis sets for the three elements Zr, Hf and O^{26,27}. For Zr and Hf, only valence electrons are treated explicitly, core electrons being described through fully relativistic effective core potentials of the Stuttgart/Cologne group. As the BS were optimized using the PW1PW functional²⁸, we chose to carry out the simulations using the same functional. Sampling of the Brillouin zone was performed through the Pack-Monkhorst method using a $(8/l) \times (8/m) \times (8/n)$ k -points grid in the reciprocal space with $l = m = n = 1$ for the pristine cells and with l and/or m and/or $n = 2$ depending on the supercell shape, e.g. $l = 2$ and $m = n = 1$ for a $2 \times 1 \times 1$ orthorhombic or monoclinic supercell and $l = m = 2$ and $n = 1$ for a $2 \times 2 \times 1$ tetragonal supercell. 10^{-10} , 10^{-10} , 10^{-10} , 10^{-12} and 10^{-24} thresholds were adopted for the Coulomb integrals overlap, Coulomb integrals penetration, Hartree-Fock exchange integrals overlap, first exchange pseudo-overlap and second exchange pseudo-overlap, respectively¹⁴.

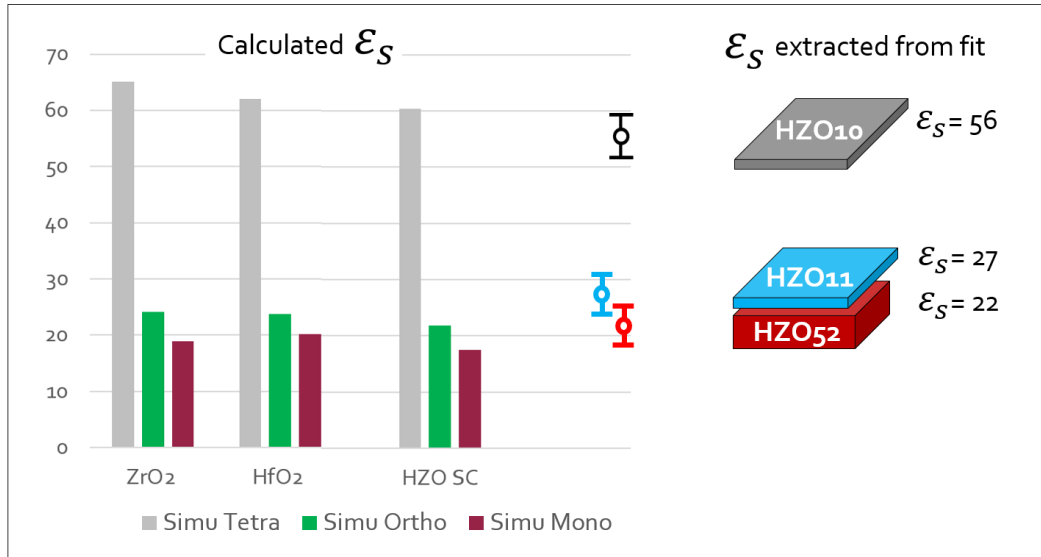


Figure 8. | Comparison of static dielectric constants ϵ_s : calculated vs extracted from IR measurements. The DFT calculated ϵ_s for pure compounds ZrO₂ and HfO₂ and for the HZO solid solution are reported as bar graphs with values for t- (gray), polar o- (green) and m- (dark red) phases. ϵ_s values extracted from broadband IR measurements using the VDF fit are reported on the right as circles with error bars : HZO10 (black), HZO21 (blue) and HZO52 (red).

Calculations were performed under symmetry constraints by considering each configuration's space group and for the supercell calculations, we forced also each configuration to remain in the original crystal system (tetragonal, orthorhombic or monoclinic) when needed. When possible, we used symmetry operations to find smaller supercells²⁹, in order to shorten the calculation time. We have named each of these configurations by a letter ranging from A to N. The space group of each configuration can be found in Table S2 of the SI. As a first step, each configuration structure was determined by optimization of its cell parameters and atomic positions, through minimization of the total energy. Each step of the optimization consisted in a self-consistent field (SCF) cycle, performed with an energy tolerance of 10^{-10} Ha. Convergence of the structural optimization procedure using the Broyden-Fletcher-Goldfarb-Shanno algorithm with the 'trust radius' method (initial value of trust radius set to 0.1 Bohr and maximum value allowed for the trust radius set to 0.3 Bohr) was considered to be achieved when all the forces, analytically calculated, were below $0.000045 \text{ Ha.Bohr}^{-1}$ and their root-mean-square (RMS) was less than $0.00003 \text{ Ha.Bohr}^{-1}$. Moreover, maximum atomic displacements between two successive steps had to be less than 0.00012 Bohr and their RMS less than 0.00018 Bohr . Last, the energy tolerance was set to 10^{-10} Ha. Note that theoretical data have not been corrected for the zero-point energy since it has negligible influence on the values of the mode frequencies.

Once all structures were optimized, the Hessian matrix elements were computed by a 3-point numerical estimate of the second derivatives of the total energy. Then, numerical diagonalization of the mass-weighted Hessian led to harmonic vibrational frequencies of the transverse optical (TO) mode at the Γ point and their IR intensities were obtained through Berry phase approach using the atomic Born tensors obtained by numerical differentiation, as implemented in the CRYSTAL code^{30,31}. The Berry phase method consists of using the atomic Born tensors, which are the derivative of the dipole moment as a function of the atomic displacements, as the differences in polarization between the central and the distorted geometries. This polarization change is then equivalent to the time-integrated transient macroscopic current that passes through the insulating material during the vibrations. Assuming Lorentzian-shape peaks for this study, we chose a full width at half maximum (FWHM) of 30 cm^{-1} since it turned out that it was the value that allowed the best comparison with the experimental data. Then, density functional perturbation theory (DFPT) was applied to compute the polarizability³²⁻³⁴. To do so, a self-consistent coupled-perturbed (SC-CP) procedure was run until the difference between the matrix elements of two SC-CP consecutive iterations is under the threshold of 10^{-4} a.u. Hence, the values of the dielectric tensor ϵ_∞ (at infinite frequency) were used for the determination of the theoretical static dielectric constants.

Grazing Incidence X-ray Diffraction

The grazing incidence x-ray diffraction (GIXRD) experiments were performed at the SixS beamline (Synchrotron SOLEIL) using a photon energy of 18.43 keV. The samples having a size of $5 \times 5 \times 0.5 \text{ mm}^3$ were measured using the UHV end-station with a background pressure in the low 10^{-10} mbar regime. For each sample, the incident angle was chosen in order to optimize

Samples	Static Dielectric Constant ϵ_s		
	Experimental	Simulated	Literature
HZO52	22	17 (m-)	16-26
HZO21	29	22 (polar o-)	25-31
HZO17	24		
HZO11	27		
HZO10	56	60 (t-)	48-70

Table 3. Different values for the static dielectric constant ϵ_s for HZO samples in multiple film thickness (52, 21, 17, 11, 10 nm). HZO10 is a mix of t- and m- phases, HZO52 is m-phase and the others are a mix of m- and polar o- phase (ferroelectric). The literature^{5,7,8,11} and simulated ϵ_s values reported for HZO10 are the ones for t-phase, for HZO11 to HZO21 are polar o-phase, and for HZO52 are the m-phase. Note that DFT simulated ϵ_s are second rank tensors represented by matrices. Each supercell configuration generates one ϵ_s matrix. Using the weighted averaged taking the Boltzmann occupation probability, $P_i(V, T)$, we obtain the averaged ϵ_s matrix for one phase. To obtain a scalar ϵ_s value, the matrices were diagonalized and the average value for the diagonal was taken for the polar o-phase and m-phase. For the t-phase, however, the ϵ_s value along the c direction (~ 60) was taken as it was closer to the experimental value (56), indicating a possible preferential orientation of the film in this direction.

the signal-to-background ratio and it was 0.14° and 0.2° for HZO11 and HZO21, respectively. A 2D hybrid pixel detector (XPAD S70) was used to collect the diffracted intensity and the BINoculars³⁵ program was used to process the whole data set (see Fig. S2 of SI).

Acknowledgements

Authors acknowledge relevant discussions and the help of David Simonne, Jean-Claude Crivello and Sébastien Junier. This work was granted access to the CCRT High-Performance Computing (HPC) facility at CEA.

Author contributions

The project has been conceptualized and supervised by P.R., J.C. and B.V. Samples have been synthesized and ferroelectric characterized by B.V, I.C.I, P.R.R. and G.S. Infrared measurements were carried out by R.C., M.V., P.H., J.B.B., and P.R. DFT calculations were performed by R.C., J.C. and E.A. The DFT and IR data treatment was performed by R.C. XRD measurements were performed by R.C., A.C., A.V., M.V., A.R., Y.G. XRD data treatment was performed by C.D., A.V., R.C., Y.G. All authors contributed to the writing of the paper.

References

1. Fan, Z., Chen, J. & Wang, J. Ferroelectric HfO₂-based materials for next-generation ferroelectric memories. *J. Adv. Dielectr.* **06**, 1630003, DOI: [10.1142/S2010135X16300036](https://doi.org/10.1142/S2010135X16300036) (2016).
2. Cheema, S. S. *et al.* Enhanced ferroelectricity in ultrathin films grown directly on silicon. *Nature* **580**, 478–482, DOI: [10.1038/s41586-020-2208-x](https://doi.org/10.1038/s41586-020-2208-x) (2020).
3. Chernikova, A. *et al.* Ultrathin Hf_{0.5}Zr_{0.5}O₂ ferroelectric films on Si. *ACS Appl. Mater. & Interfaces* **8**, 7232–7237, DOI: [10.1021/acsami.5b11653](https://doi.org/10.1021/acsami.5b11653) (2016).
4. Cojocaru, B. *et al.* Phase control in hafnia: New synthesis approach and convergence of average and local structure properties. *ACS Omega* **4**, 8881–8891, DOI: [10.1021/acsomega.9b00580](https://doi.org/10.1021/acsomega.9b00580) (2019).
5. Park, M. H. *et al.* A comprehensive study on the structural evolution of HfO₂ thin films doped with various dopants. *J. Mater. Chem. C* **5**, 4677–4690, DOI: [10.1039/C7TC01200D](https://doi.org/10.1039/C7TC01200D) (2017).
6. Gong, N. & Ma, T.-P. Why is FEHfO₂ more suitable than PZT or SBT for scaled nonvolatile 1-T memory cell? A retention perspective. *IEEE Electron Device Lett.* **37**, 1123–1126, DOI: [10.1109/LED.2016.2593627](https://doi.org/10.1109/LED.2016.2593627) (2016).
7. Materlik, R., Künneth, C. & Kersch, A. The origin of ferroelectricity in Hf_{1-x}Zr_xO₂: A computational investigation and a surface energy model. *J. Appl. Phys.* **117**, 134109, DOI: [10.1063/1.4916707](https://doi.org/10.1063/1.4916707) (2015).
8. Zhao, X. & Vanderbilt, D. First-principles study of structural, vibrational, and lattice dielectric properties of hafnium oxide. *Phys. Rev. B* **65**, 233106, DOI: [10.1103/PhysRevB.65.233106](https://doi.org/10.1103/PhysRevB.65.233106) (2002).
9. Delodovici, F., Barone, P. & Picozzi, S. Trilinear-coupling-driven ferroelectricity in HfO₂. *Phys. Rev. Mater.* **5**, 064405, DOI: [10.1103/PhysRevMaterials.5.064405](https://doi.org/10.1103/PhysRevMaterials.5.064405) (2021).
10. Bösecke, T. S., Müller, J., Bräuhaus, D., Schröder, U. & Böttger, U. Ferroelectricity in hafnium oxide thin films. *Appl. Phys. Lett.* **99**, 102903, DOI: [10.1063/1.3634052](https://doi.org/10.1063/1.3634052) (2011).
11. Park, M. H. *et al.* Review of defect chemistry in fluorite-structure ferroelectrics for future electronic devices. *J. Mater. Chem. C* **8**, 10526–10550, DOI: [10.1039/D0TC01695K](https://doi.org/10.1039/D0TC01695K) (2020).
12. Müller, J. *et al.* Ferroelectricity in simple binary ZrO₂ and HfO₂. *Nano Lett.* **12**, 4318–4323, DOI: [10.1021/nl302049k](https://doi.org/10.1021/nl302049k) (2012).
13. Fan, S. *et al.* Vibrational fingerprints of ferroelectric HfO₂. *npj Quantum Mater.* **7**, 32, DOI: [10.1038/s41535-022-00436-8](https://doi.org/10.1038/s41535-022-00436-8) (2022).
14. Dovesi, R. *et al.* Quantum-mechanical condensed matter simulations with CRYSTAL. *WIREs Comput. Mol. Sci.* **8**, e1360, DOI: <https://doi.org/10.1002/wcms.1360> (2018).
15. Boutaybi, A. E. *et al.* Ferroelectric ZrO₂ phases from infrared spectroscopy. *J. Mater. Chem. C* **11**, 10931–10941, DOI: [10.1039/D3TC01985C](https://doi.org/10.1039/D3TC01985C) (2023).
16. Cervasio, R. *et al.* IR spectroscopy of PbZr_{1-x}Ti_xO₃ material: A complementary experimental/*Ab Initio* calculations approach of a solid solution. *The J. Phys. Chem. C* **126**, 12860–12869, DOI: [10.1021/acs.jpcc.2c03046](https://doi.org/10.1021/acs.jpcc.2c03046) (2022).
17. Peperstraete, Y., Emilie, A., Tétot, R. & Roy, P. *Ab initio* study for the IR spectroscopy of PbTiO₃ and PbZrO₃, primary blocks of Pb_{1-x}Zr_xO₃. *J. physics. Condens. matter: an Inst. Phys. journal* **30**, 215702, DOI: [10.1088/1361-648X/aabcff](https://doi.org/10.1088/1361-648X/aabcff) (2018).
18. Mustapha, S. *et al.* On the use of symmetry in configurational analysis for the simulation of disordered solids. *J. Physics: Condens. Matter* **25**, 105401, DOI: [10.1088/0953-8984/25/10/105401](https://doi.org/10.1088/0953-8984/25/10/105401) (2013).
19. DARCO, P. *et al.* Symmetry and random sampling of symmetry independent configurations for the simulation of disordered solids. *J. Physics: Condens. Matter* **25**, 355401, DOI: [10.1088/0953-8984/25/35/355401](https://doi.org/10.1088/0953-8984/25/35/355401) (2013).
20. De La Pierre, M. *et al.* The infrared vibrational spectrum of andradite-grossular solid solutions: A quantum mechanical simulation. *Am. Mineral.* **98**, 966–976, DOI: [10.2138/am.2013.4156](https://doi.org/10.2138/am.2013.4156) (2013).
21. Basri, K. N. *et al.* FT-NIR, MicroNIR and LED-MicroNIR for detection of adulteration in palm oil via PLS and LDA. *Anal. Methods* **10**, 4143–4151, DOI: [10.1039/C8AY01239C](https://doi.org/10.1039/C8AY01239C) (2018).
22. Rao, Y. *et al.* Quantitative and qualitative determination of acid value of peanut oil using near-infrared spectrometry. *J. Food Eng.* **93**, 249–252, DOI: [10.1016/j.jfoodeng.2009.01.023](https://doi.org/10.1016/j.jfoodeng.2009.01.023) (2009).
23. RefFIT: Fitting optical spectra.

24. Kuzmenko, A. B. KramersKronig constrained variational analysis of optical spectra. *Rev. Sci. Instruments* **76**, 083108, DOI: [10.1063/1.1979470](https://doi.org/10.1063/1.1979470) (2005).
25. Roy, P., Rouzières, M., Qi, Z. & Chubar, O. The AILES Infrared Beamline on the third generation Synchrotron Radiation Facility SOLEIL. *Infrared Phys. & Technol.* **49**, 139–146, DOI: [10.1016/j.infrared.2006.01.015](https://doi.org/10.1016/j.infrared.2006.01.015) (2006).
26. Vilela Oliveira, D., Laun, J., Peintinger, M. F. & Bredow, T. BSSE-correction scheme for consistent gaussian basis sets of double- and triple-zeta valence with polarization quality for solid-state calculations. *J. Comput. Chem.* **40**, 2364–2376, DOI: <https://doi.org/10.1002/jcc.26013> (2019).
27. Laun, J. & Bredow, T. BSSE-corrected consistent gaussian basis sets of triple-zeta valence with polarization quality of the fifth period for solid-state calculations. *J. Comput. Chem.* **43**, 839–846, DOI: <https://doi.org/10.1002/jcc.26839> (2022).
28. Bredow, T. & Gerson, A. R. Effect of exchange and correlation on bulk properties of MgO, NiO, and CoO. *Phys. Rev. B* **61**, 5194–5201, DOI: [10.1103/PhysRevB.61.5194](https://doi.org/10.1103/PhysRevB.61.5194) (2000).
29. Stokes, H. T. & Hatch, D. M. *FINDSYM*: program for identifying the space-group symmetry of a crystal. *J. Appl. Crystallogr.* **38**, 237–238, DOI: [10.1107/S0021889804031528](https://doi.org/10.1107/S0021889804031528) (2005).
30. Pascale, F. *et al.* The calculation of the vibrational frequencies of crystalline compounds and its implementation in the CRYSTAL code. *J. Comput. Chem.* **25**, 888–897, DOI: <https://doi.org/10.1002/jcc.20019> (2004).
31. Zicovich-Wilson, C. M. *et al.* Calculation of the vibration frequencies of alpha-quartz: The effect of hamiltonian and basis set. *J. Comput. Chem.* **25**, 1873–1881, DOI: <https://doi.org/10.1002/jcc.20120> (2004).
32. Ferrero, M., Rérat, M., Orlando, R. & Dovesi, R. Coupled perturbed hartree-fock for periodic systems: The role of symmetry and related computational aspects. *The J. Chem. Phys.* **128**, 014110, DOI: [10.1063/1.2817596](https://doi.org/10.1063/1.2817596) (2008).
33. Ferrero, M., Rérat, M., Orlando, R. & Dovesi, R. The calculation of static polarizabilities of 1-3D periodic compounds. the implementation in the crystal code. *J. Comput. Chem.* **29**, 1450–1459, DOI: <https://doi.org/10.1002/jcc.20905> (2008).
34. Ferrero, M., Rérat, M., Kirtman, B. & Dovesi, R. Calculation of first and second static hyperpolarizabilities of one- to three-dimensional periodic compounds. implementation in the CRYSTAL code. *The J. Chem. Phys.* **129**, 244110, DOI: [10.1063/1.3043366](https://doi.org/10.1063/1.3043366) (2008).
35. Roobol, S., Onderwaater, W., Drnec, J., Felici, R. & Frenken, J. *BINoculars* : data reduction and analysis software for two-dimensional detectors in surface X-ray diffraction. *J. Appl. Crystallogr.* **48**, 1324–1329, DOI: [10.1107/S1600576715009607](https://doi.org/10.1107/S1600576715009607) (2015).

Supplementary information

Some additional data about (1) Ferroelectric P-E Loop; (2) XRD diffractograms for HZO11 and HZO21 samples at room-temperature with theoretical polar o-phase, t-phase and m-phase peak positions generated from a CIF file ; (3) FIR absorbance spectra normalized for all HZO films (4) Extraction of optical functions for all 5 films; (5) Dielectric loss function extracted from the Variational Dielectric Function fit (VDF) using the REFFIT software; (6) Table S1 : parameters based in a Drude-Lorentz oscillator function for the Variational Dielectric Function fit ; (7) Table S2: Space groups for all configurations of the t-, polar o- and m- phases; (8) Fig. S6: Different mixing compositions for two HZO phases: o-phase and m-phase, ranging from 100% to 0% m-phase; (9) Fig. S7 Different mixing compositions for two HZO phases: t-phase and m-phase, ranging from 100% to 0% m-phase; (10) S8 to S16 : DFT IR spectra for all supercell for t, o, m-phases in all 3 directions; (11) Figures S17 to S19: crystal structures for t-, m- and polar o-phases in three configurations denoting how the two mixed atoms Zr and Hf are labeled; (12) Tables for t-, polar o- and m- phases with all configurations, schemes for the positions of Zr and Hf atoms, energies, multiplicities and population percentages.

Ferroelectric P-E Loop

Fig. S1 shows the ferroelectric polarisation vs electric field loop. To verify the ferroelectric aspect of the films, the same deposition method was carried on doped Si, and a extra TiN layer was deposited on top of the HZO film, in order to have the necessary electrodes to probe the hysteresis loop.

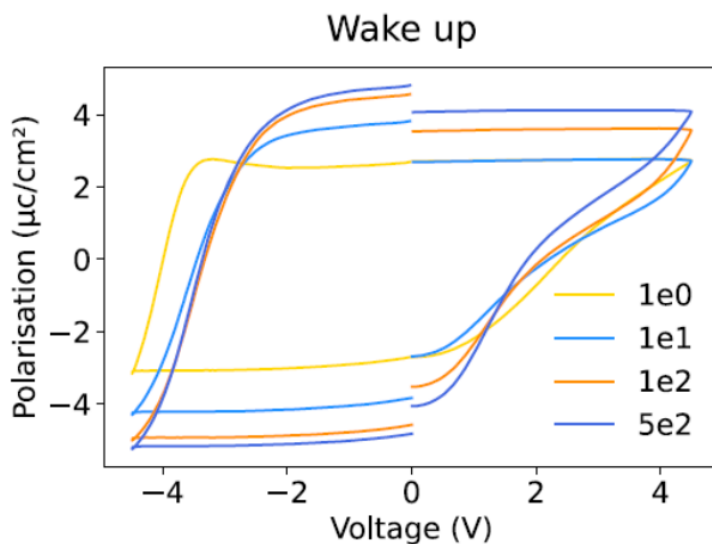


Figure S1. | Ferroelectric polarisation vs electric field loop. Results are shown for multiple cycles

Experimental XRD

Fig. S2 shows the XRD diffractograms for HZO11 and HZO21 samples at room-temperature. The blue lines mark the theoretical polar o-phase peak positions, whereas the red ones are the m-phase peak positions generated from a CIF file.

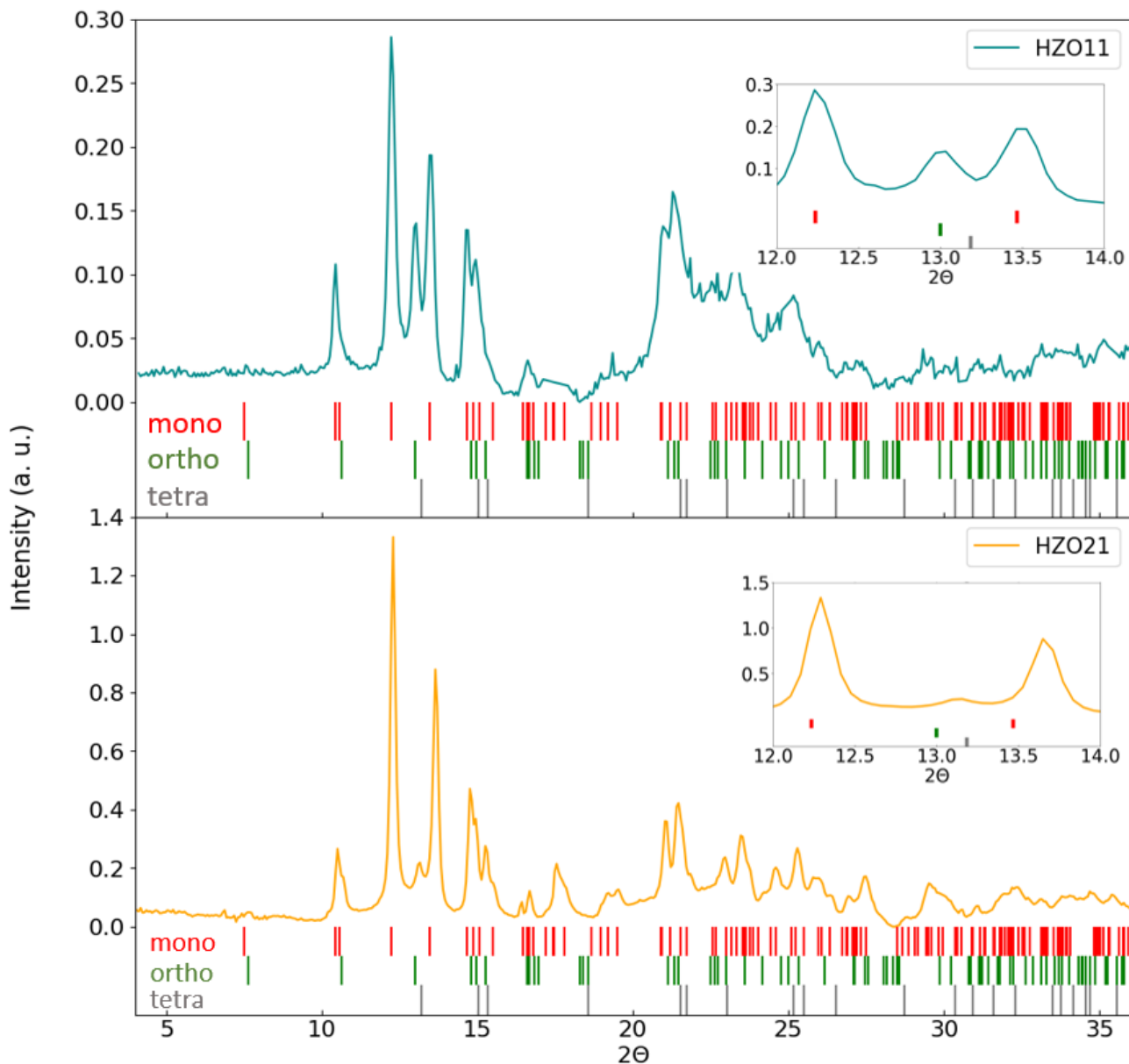


Figure S2. | XRD diffractograms for HZO11 and HZO21. The red vertical lines show the theoretical m-phase, whereas the green ones are the polar o-phase and the gray ones are the t-phase peak positions respectively.

Experimental IR

Fig. S3 shows the FIR spectra for all thickness with absorbance normalized to 1.

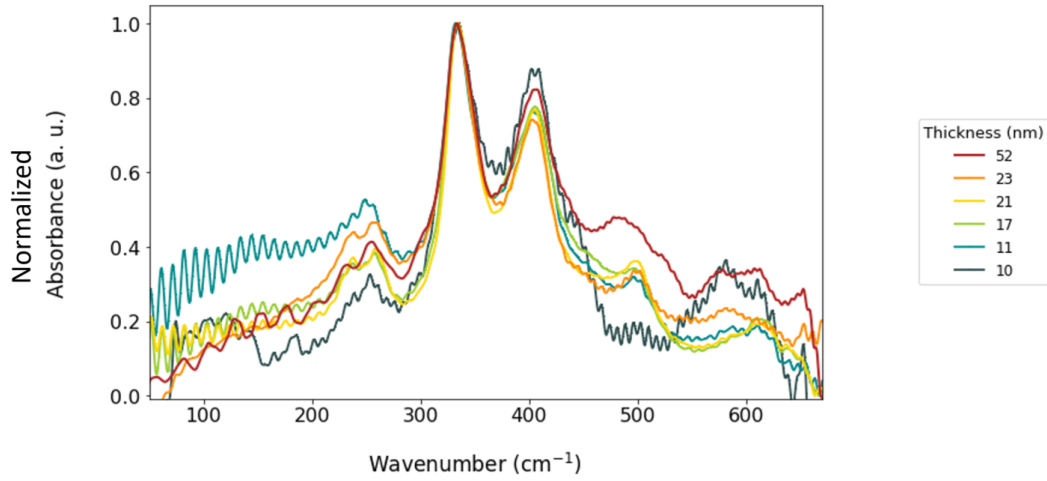


Figure S3. | IR absorption measurements for all HZO thickness normalized to 1. Results are shown in normalized absorbance scale (a. u.) and help to clarify the different phonons signatures from each sample.

Extraction of Optical Functions

Fig. S4 shows the complex dielectric function (ϵ_1 and ϵ_2), complex refractive index (n and k) and the complex conductivity functions (σ_1 and σ_2) for HZO10, HZO11, HZO17 and HZO52.

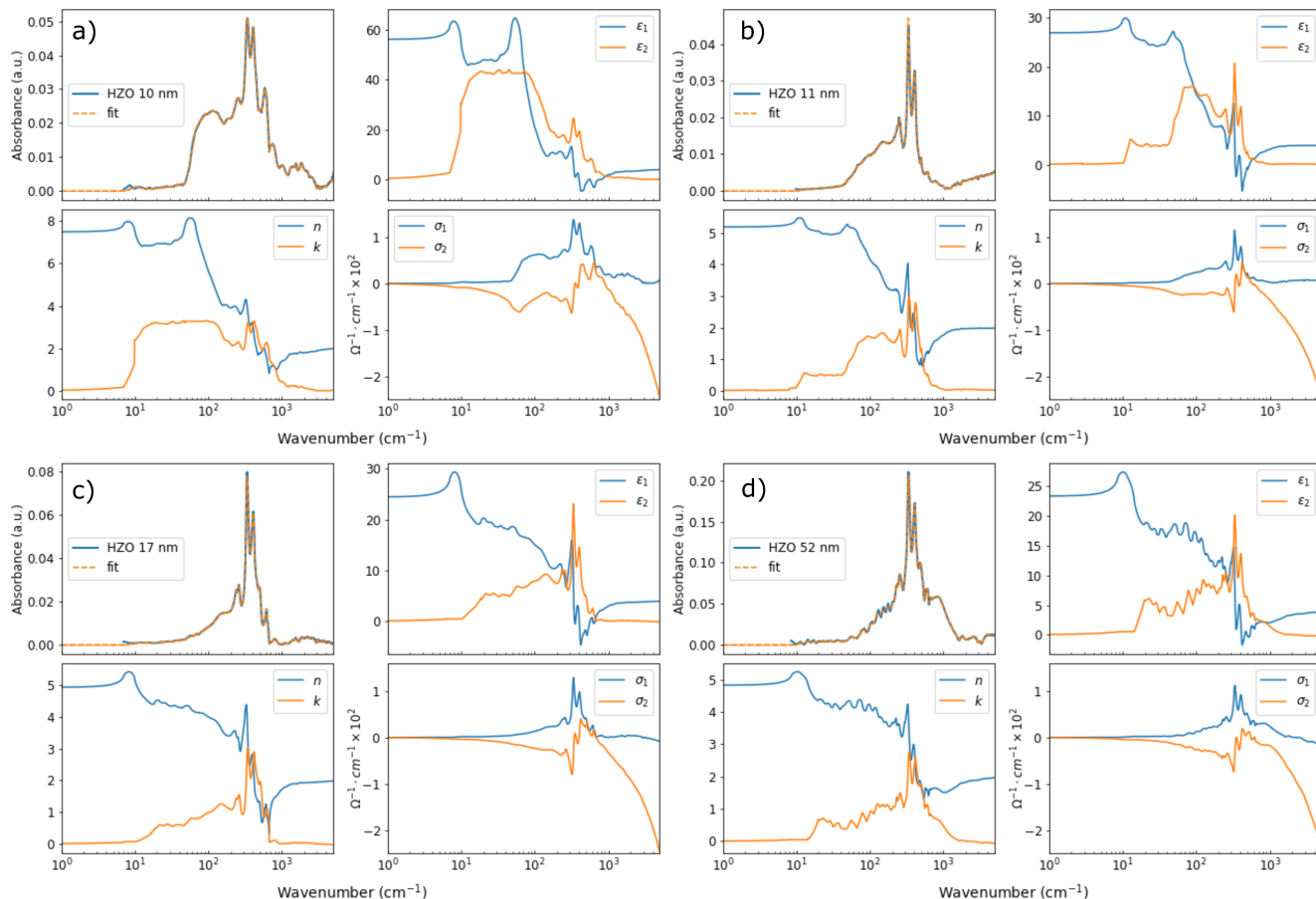


Figure S4. Each panel displays the absorbance data and its fit, the dielectric function, refractive index and optical conductivity for (a) HZO10; (b) HZO11; (c) HZO17; (d) HZO52.

Fig. S5 shows the absorbance spectra together with the dielectric loss function $-\text{Im}(1/\epsilon) = \epsilon_2/(\epsilon_1^2 + \epsilon_2^2)$, extracted from the *Variational Dielectric Function* (VDF) fit²⁴ using the REFFIT software²³. Table S1 reports the starting-point parameters based in a Drude-Lorentz oscillator function for the VDF algorithm.

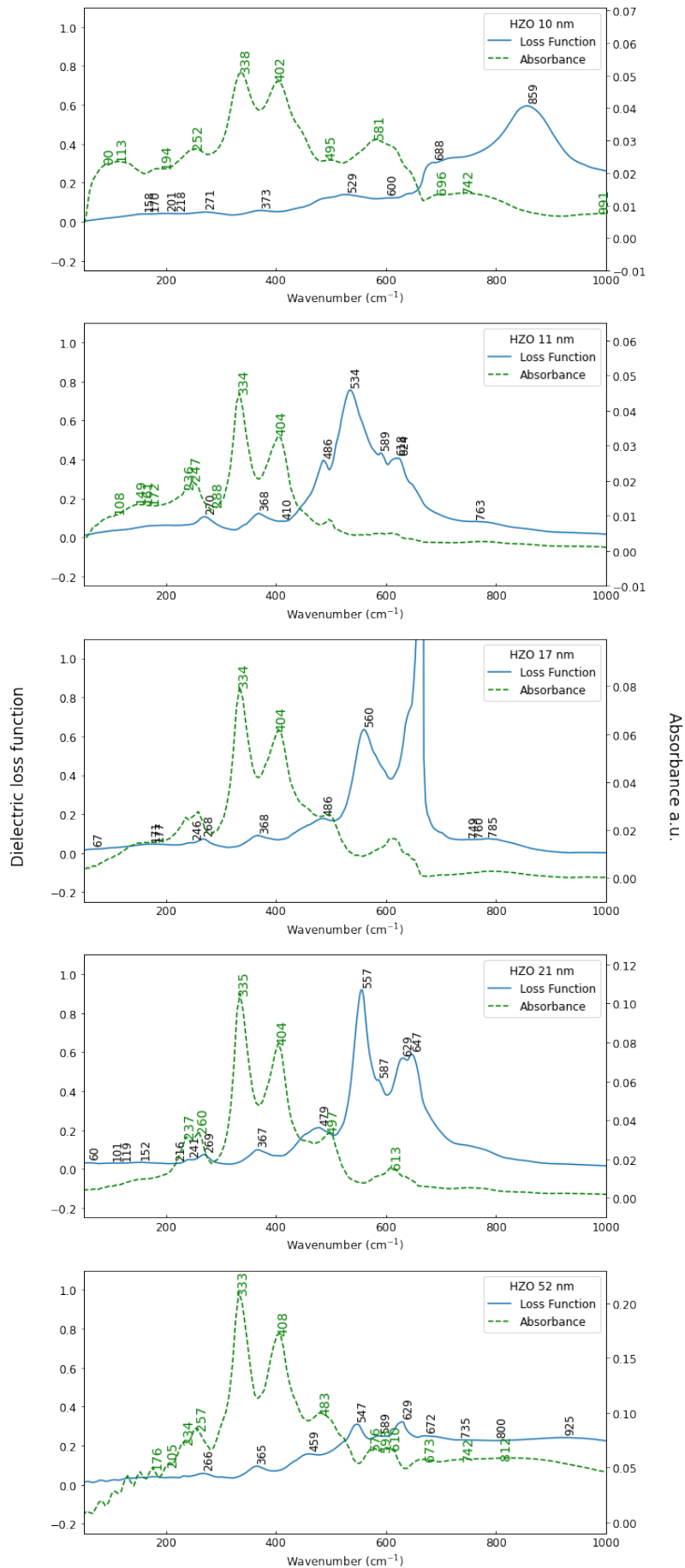


Figure S5. Dielectric loss function (blue curves, left vertical axis) and absorbance data (green dashed curves, right vertical axis) for all sample thickness.

Sample	ω_0	ω_p	Γ
HZO10	100	594	101
	190	403	97
	250	389	66
	335	614	61
	406	648	73
	500	376	84
	591	600	97
	760	543	215
	1040	537	351
HZO11	154	580	167
	230	123	18
	255	215	31
	331	334	21
	404	540	68
	510	163	53
	610	107	28
HZO17	160	483	181
	235	166	29
	260	140	23
	335	573	53
	406	551	68
	500	301	62
	610	237	51
	800	75	48
HZO21	157	325	153
	235	148	17
	260	241	31
	335	462	31
	400	520	51
	500	378	71
	610	164	34
HZO52	154	442	152
	228	92	11
	255	254	41
	332	463	39
	406	478	51
	485	415	84
	574	93	21
	619	347	110
	851	839	423

Table S1. Starting-point parameters based in a Drude-Lorentz oscillator function for the Variational Dielectric Function algorithm.

DFT Calculations

Configuration	Tetragonal (t-, 137 $P4_2/nmc$)			Orthorhombic (polar o-, 29 $Pca2_1$)			Monoclinic (m-, 14 $P2_1/c$)		
	122	212	221	112	121	211	112	121	211
A	$P2_1/m$	$P2_1/m$	$P2_1/m$	Pc	P1	Pc	$P2_1$	Pc	P1
B	Pm	Pm	P1	P1	P1	P1	P1	P1	P1
C	Pmm2	Pmm2	$P4_2mc$	P1	P1	P1	P1	P1	P1
D	Pm	Pm	P1	P1	P1	P1	P1	P1	P1
E	$Pmc2_1$	$Pmc2_1$	P1	P1	P1	$P2_1$	P1	P1	P1
F	Pmmn	Pmmn	$P\bar{4}m2$	P1	$P2_1$	P1	P1	P1	P1
G	Pmm2	Pmm2		P1	P1	P1	P1	P1	P1
H	P1	P1		$P2_1$	P1	$P2_1$	P1	P1	P1
I	$P\bar{4}m2$	$P\bar{4}m2$		P1	$Pna2_1$	$P2_1$	P1	P1	P1
J	Pmmn	Pmmn		Pc	Pc	$P2_1$	$P2_1$	$P2_1$	$P2_1$
K				Pc	P1	P1	P1	P1	P1
L				Pc	P1	Pc	$P2_1$	Pc	P1
M					Pc	Pc	Pc	Pc	P1
N					$Pna2_1$				P1

Table S2. Space groups for all configurations of the t-, polar o- and m- phases.

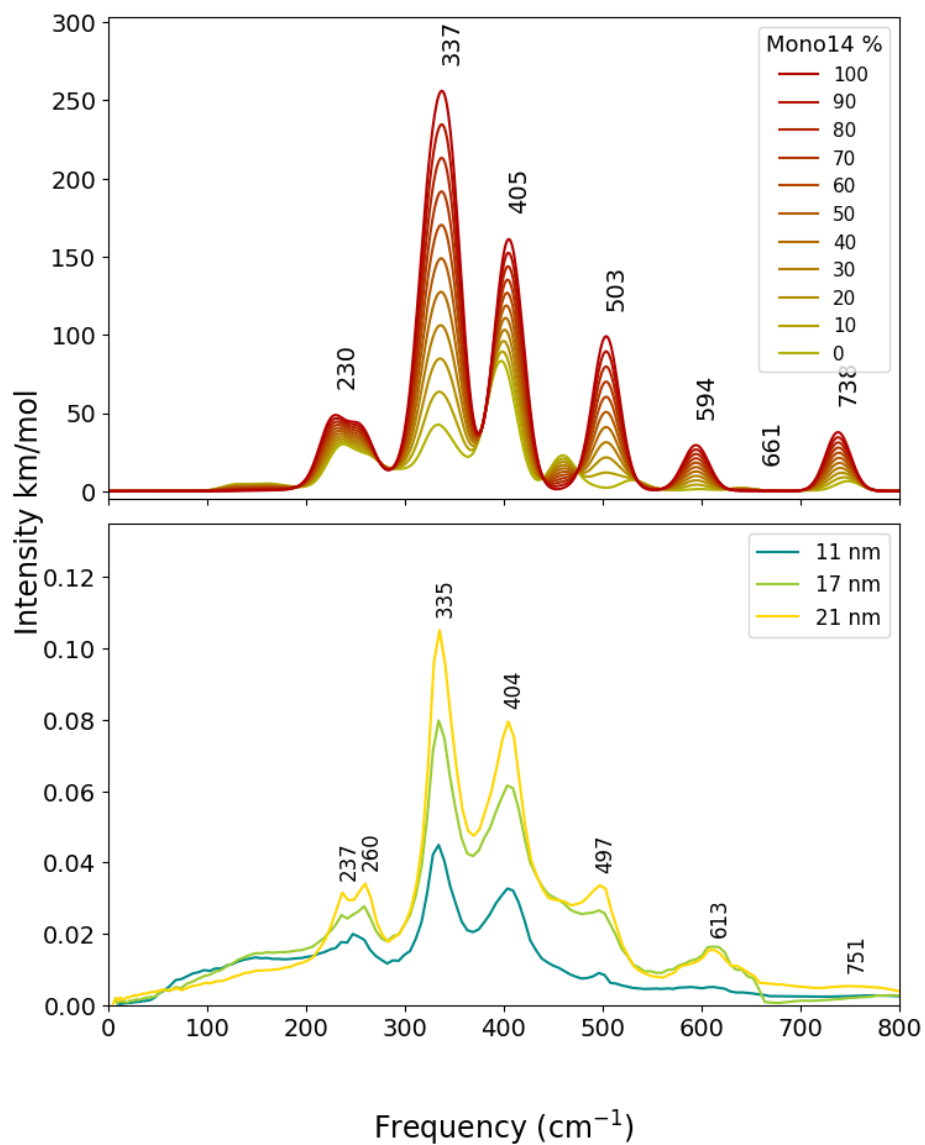


Figure S6. Different mixing compositions for two HZO phases: o-phase and m-phase, ranging from 100% to 0% m-phase. Both theoretical spectra has their intensities normalized to the 3-atom elemental unit HfZrO₂.

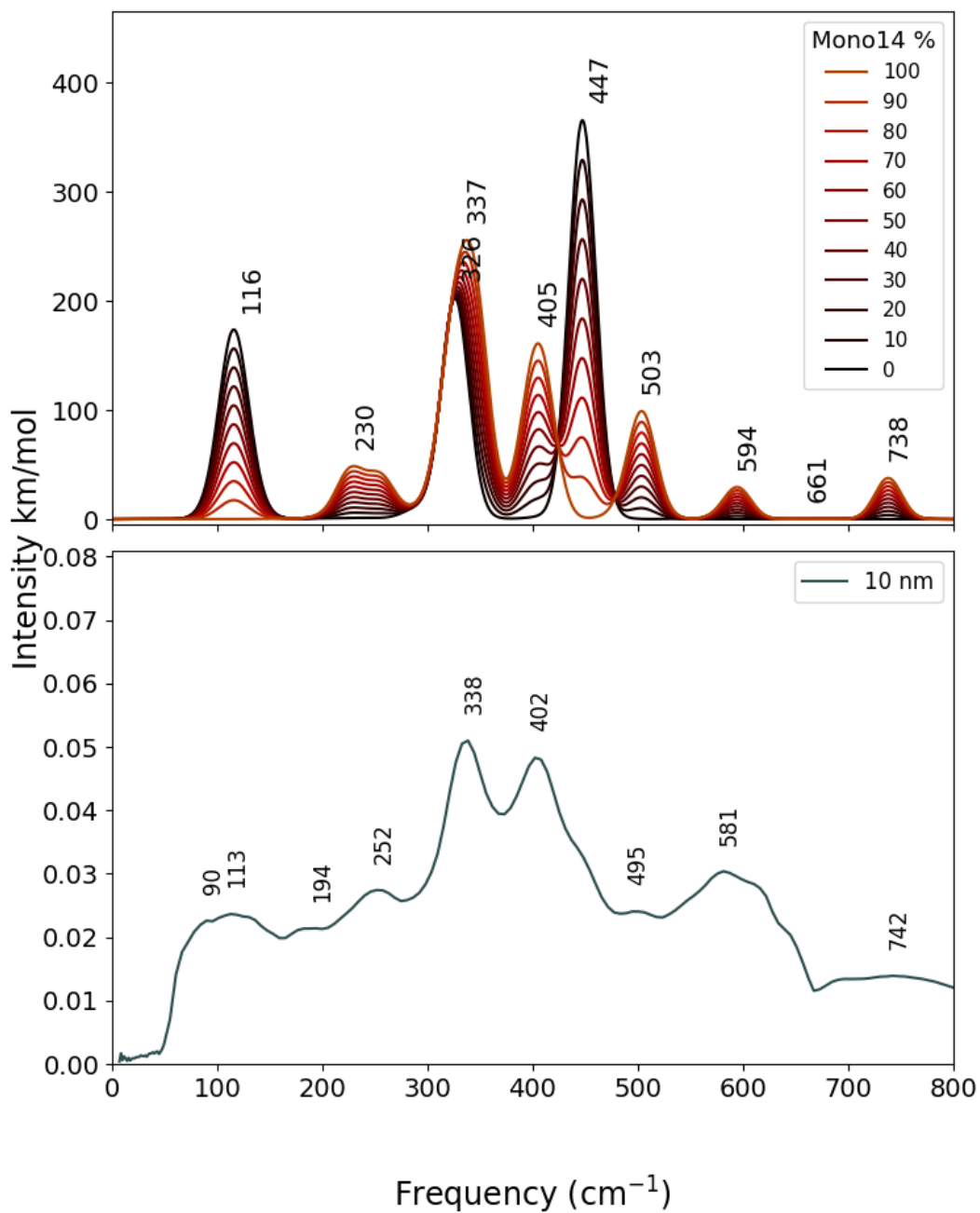


Figure S7. Different mixing compositions for two HZO phases: t-phase and m-phase, ranging from 100% to 0% m-phase. Both theoretical spectra has their intensities normalized to the 3-atom elemental unit HfZrO_2 .

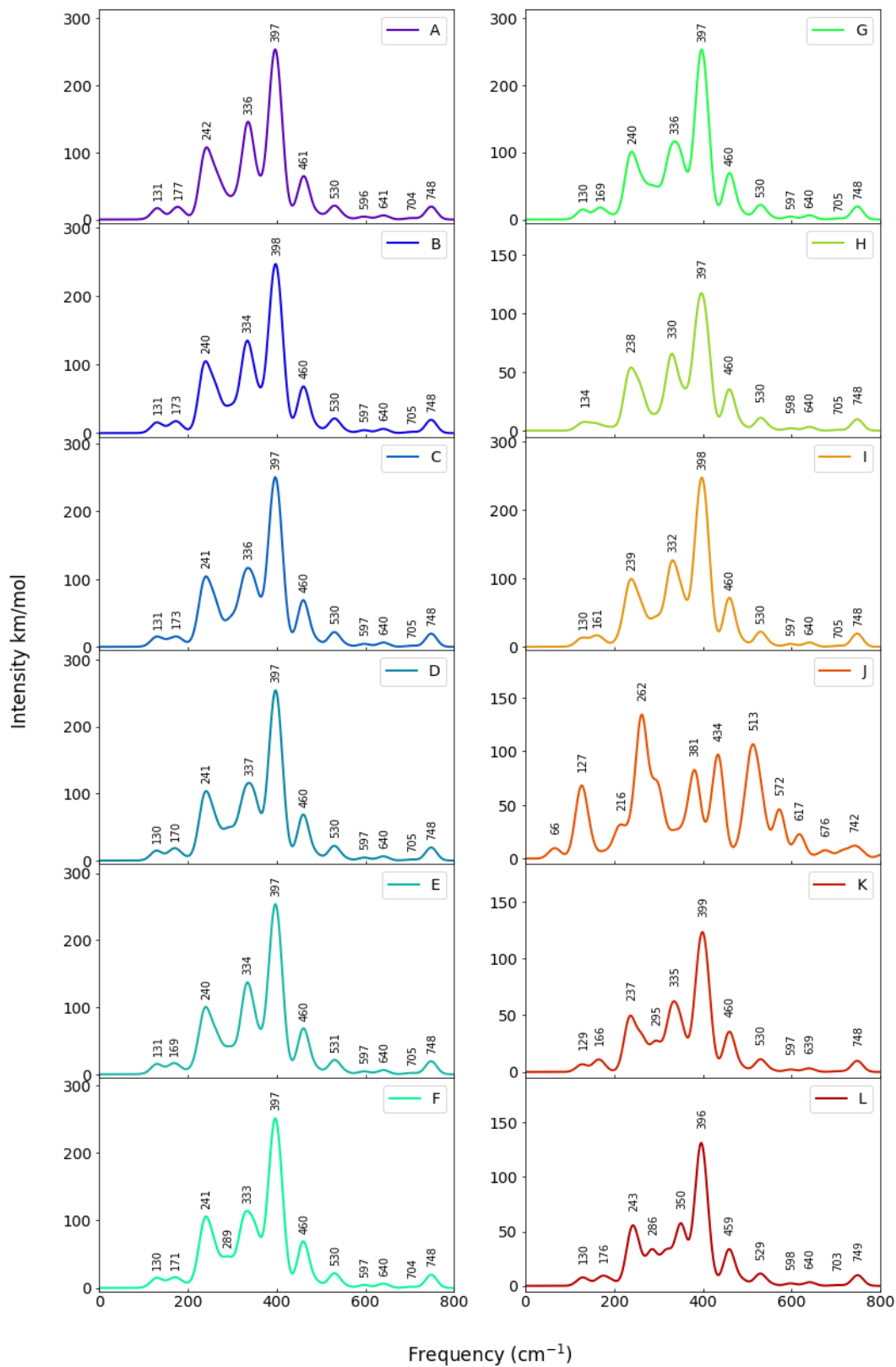


Figure S8. DFT IR spectra for all supercell configurations of the polar o-phase in the 1x1x2 direction.

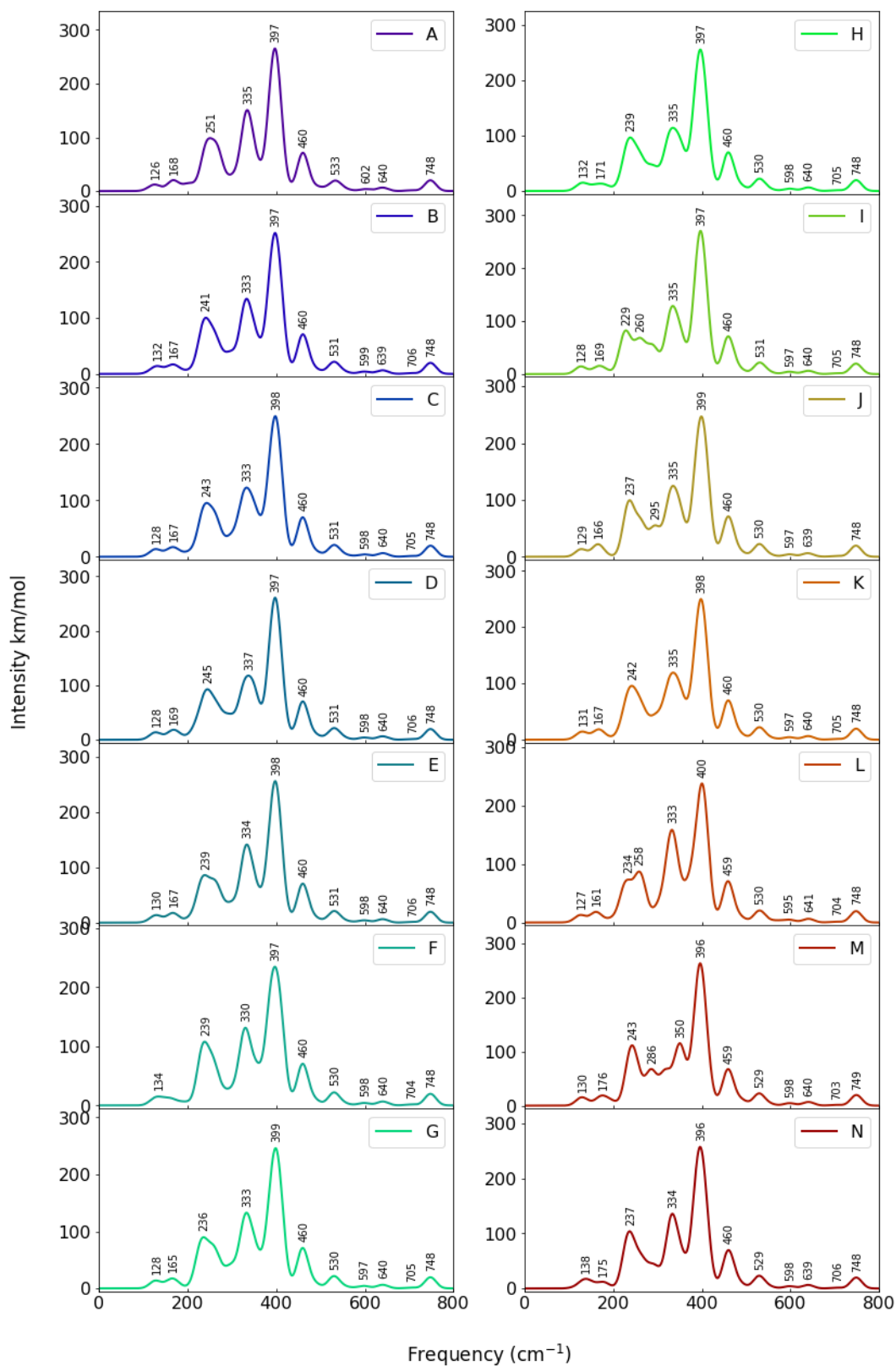


Figure S9. DFT IR spectra for all supercell configurations of the polar o-phase in the 1x2x1 direction.

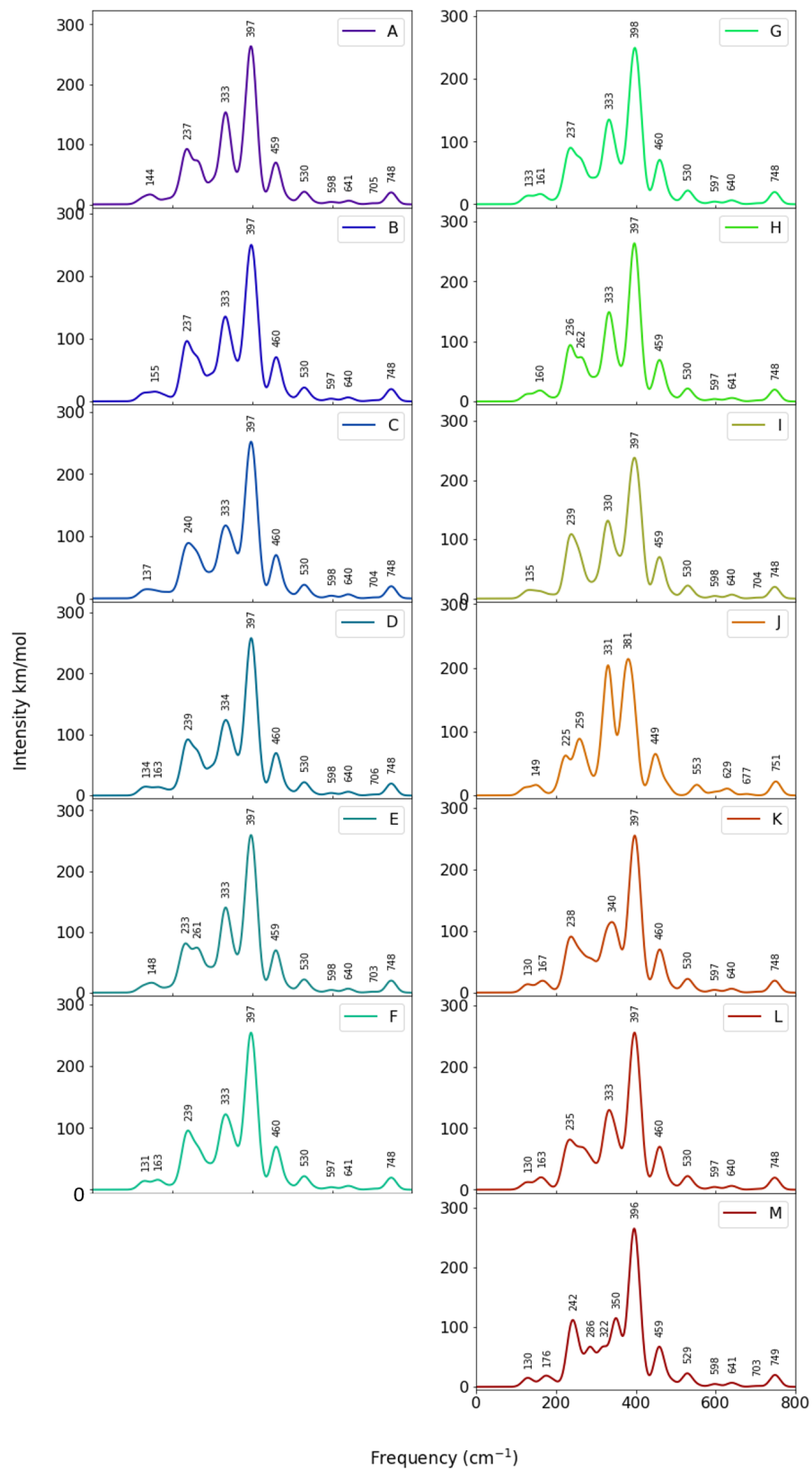


Figure S10. DFT IR spectra for all supercell configurations of the polar o-phase in the 2x1x1 direction.

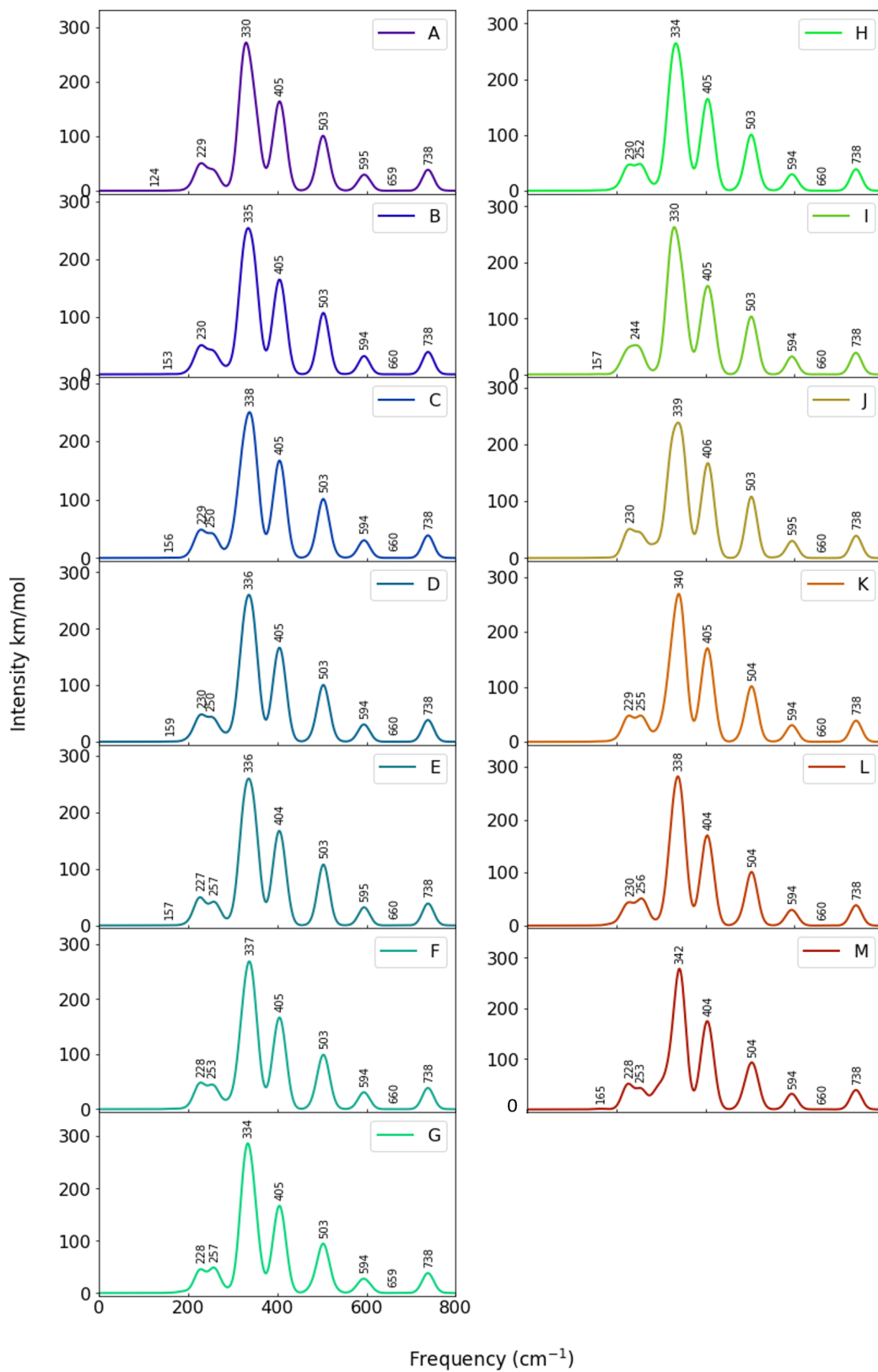


Figure S11. DFT IR spectra for all supercell configurations of the m-phase in the 1x1x2 direction.

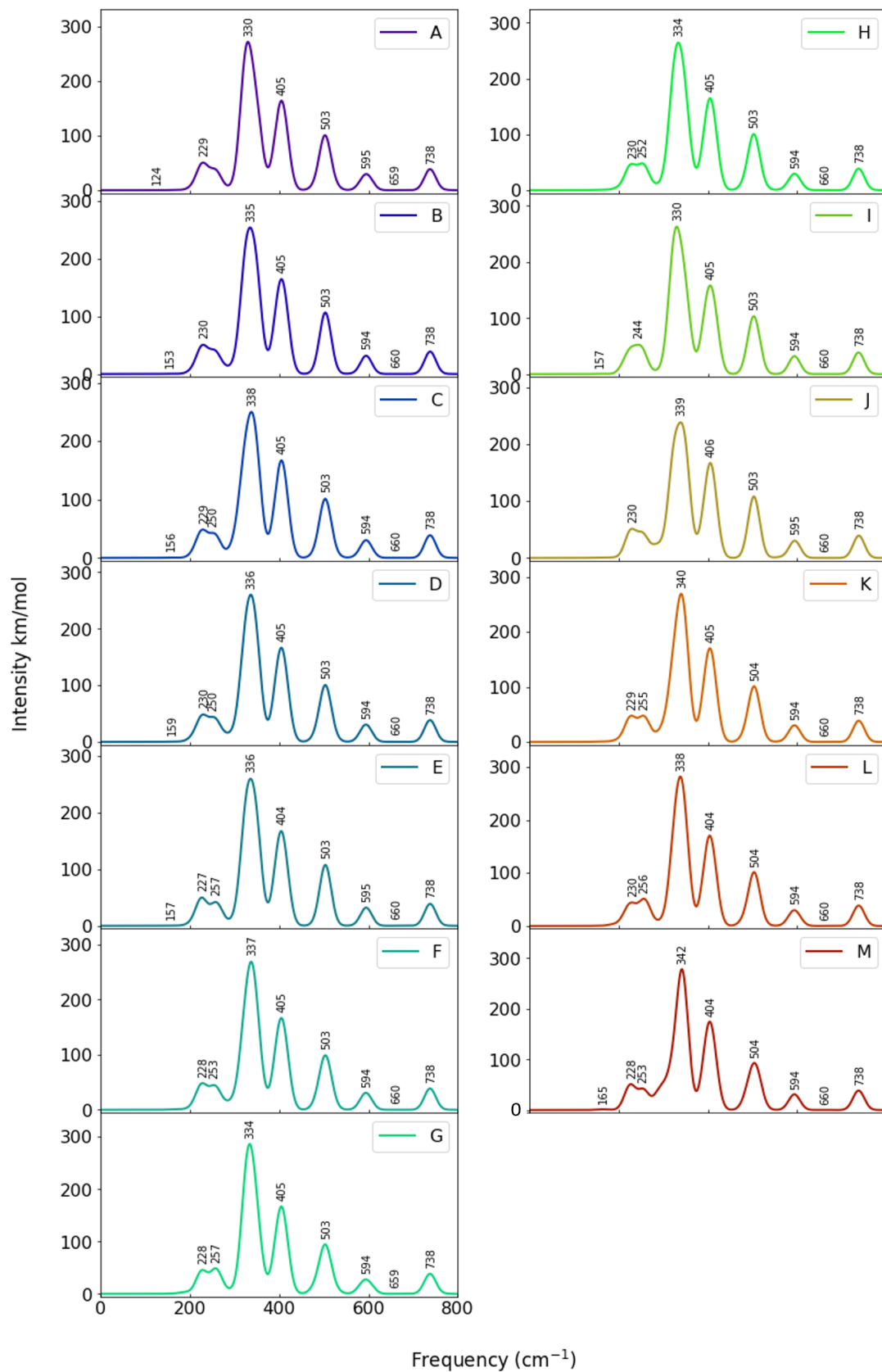


Figure S12. DFT IR spectra for all supercell configurations of the m-phase in the 1x2x1 direction.

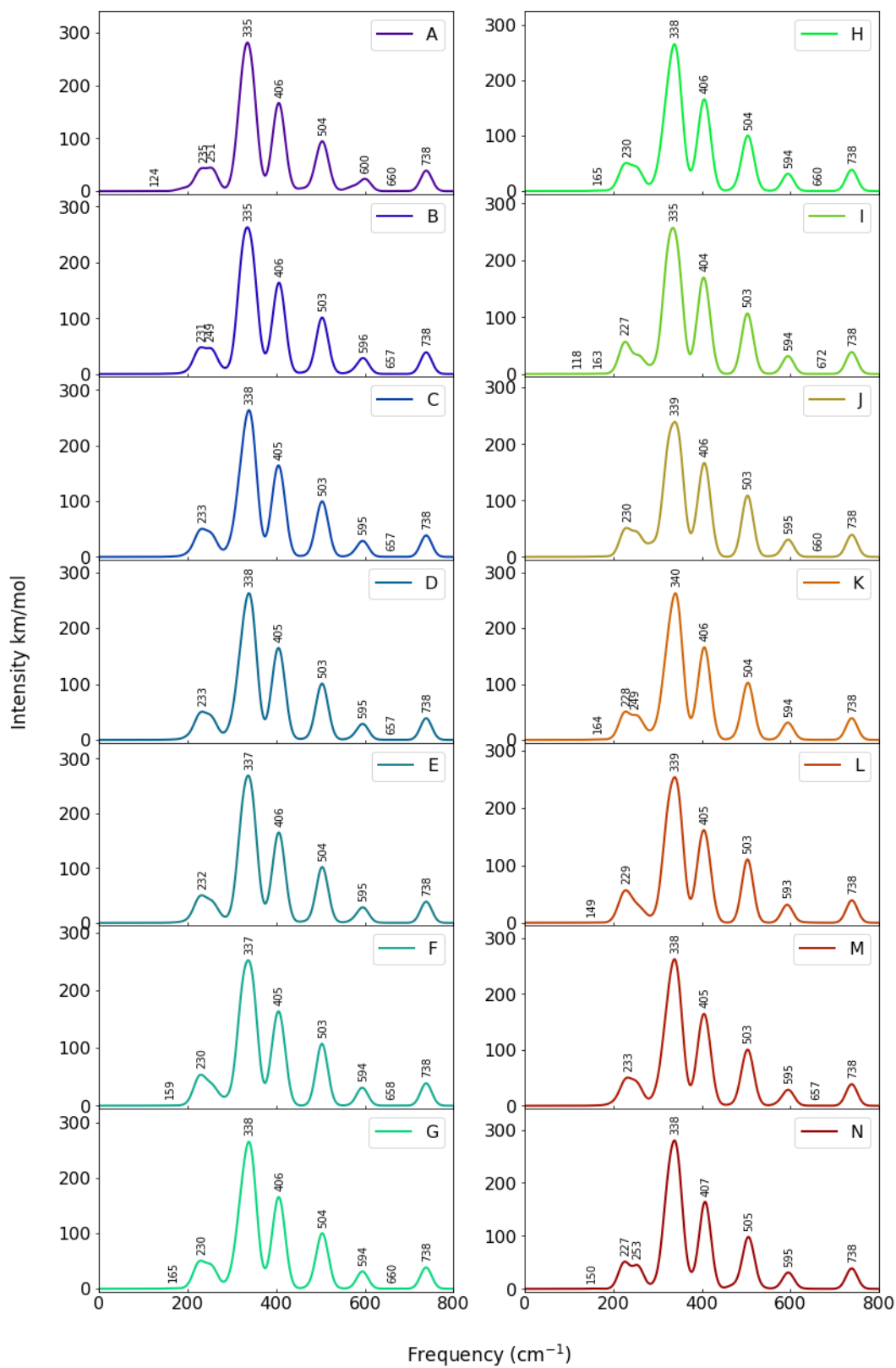


Figure S13. DFT IR spectra for all supercell configurations of the m-phase in the 2x1x1 direction.

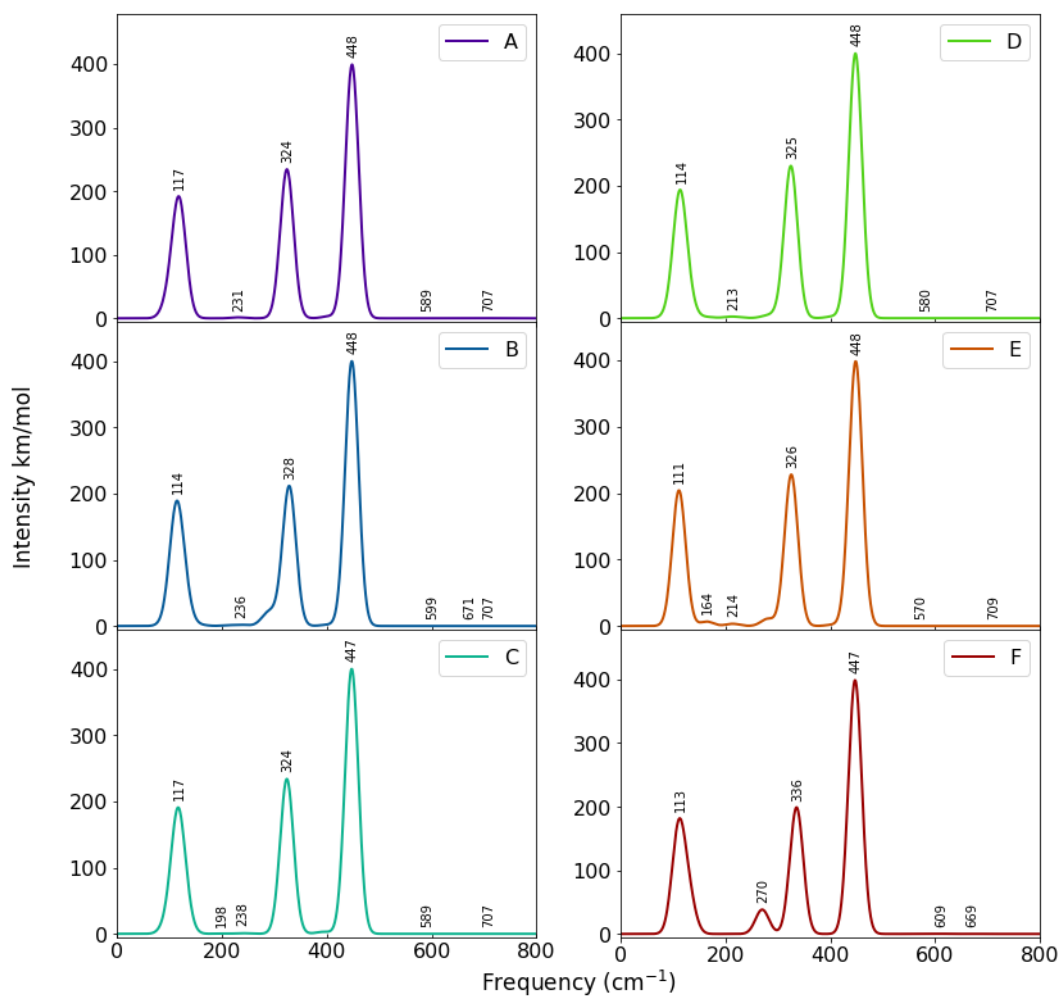


Figure S14. DFT IR spectra for all supercell configurations of the t-phase in the 2x2x1 direction.

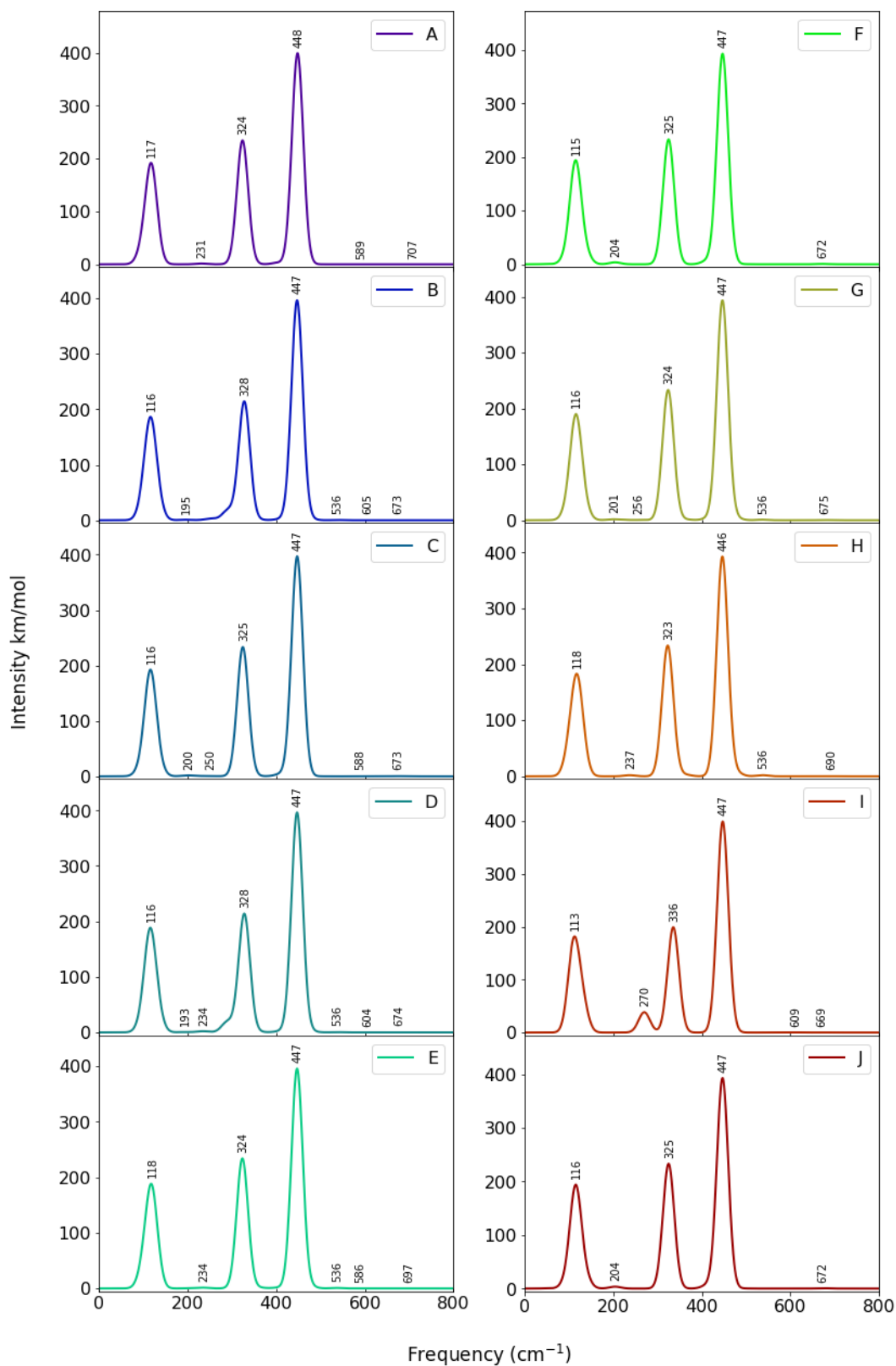


Figure S15. DFT IR spectra for all supercell configurations of the t-phase in the 2x1x2 direction.

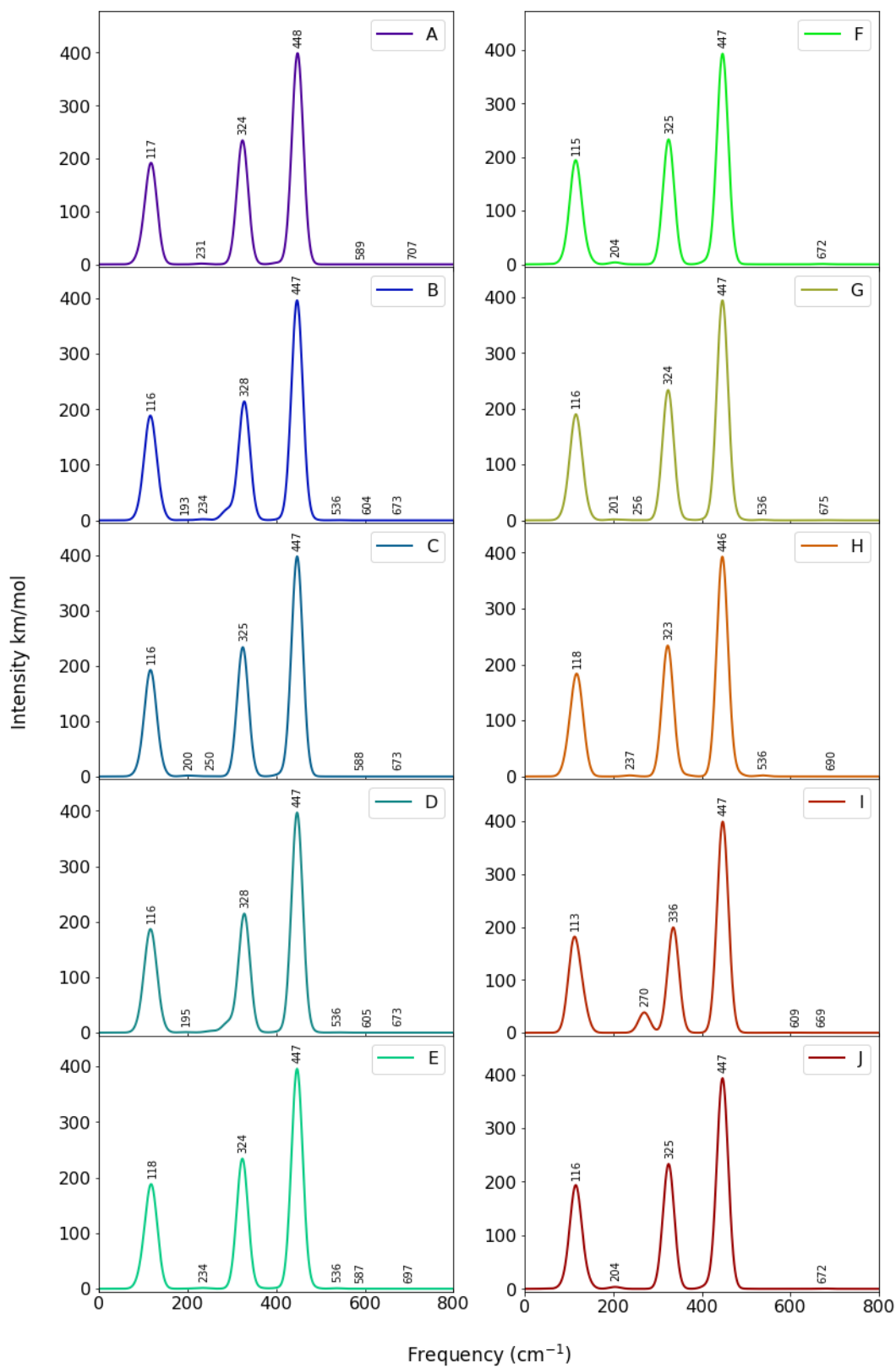


Figure S16. DFT IR spectra for all supercell configurations of the t-phase in the 1x2x2 direction.

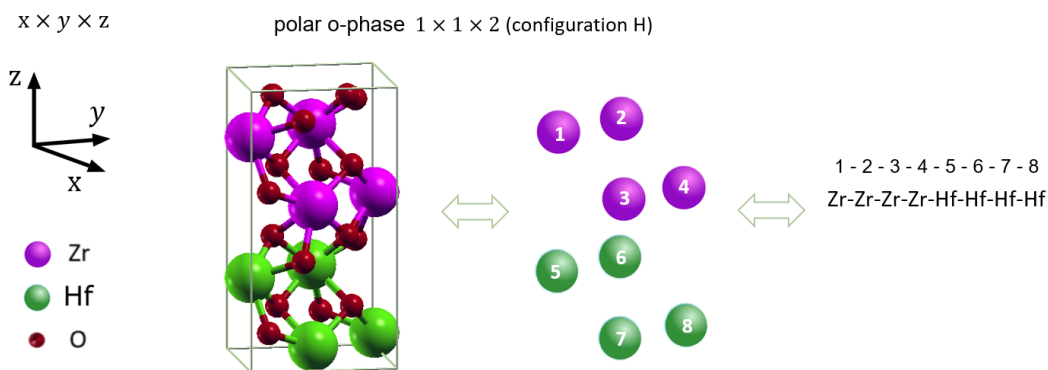


Figure S17. Crystal structure for the polar o-phase HZO in the $1 \times 1 \times 2$ direction in space, for configuration H (see Table S3). The scheme denotes how the two mixed atoms Zr and Hf are labeled and give rise to the different configurations possible of the HZO solid solution.

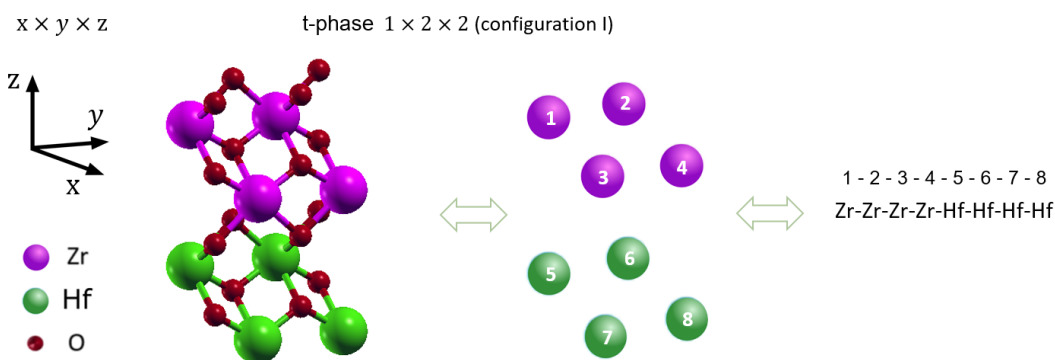


Figure S18. Crystal structure for the t-phase HZO in the $1 \times 2 \times 2$ direction in space, for configuration I (see Table S4). The crystal structure is represented here in this asymmetric unit. The scheme denotes how the two mixed atoms Zr and Hf are labeled and give rise to the different configurations possible of the HZO solid solution.

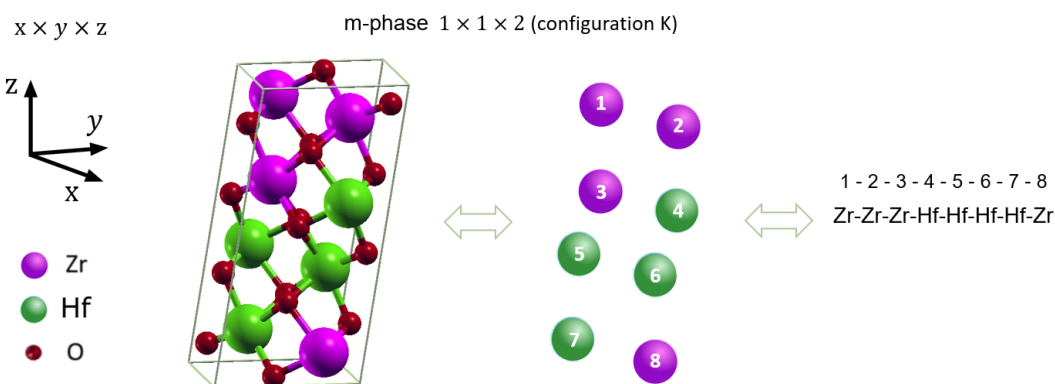


Figure S19. Crystal structure for the m-phase HZO in the $1 \times 1 \times 2$ direction in space, for configuration K (see Table S5). The scheme denotes how the two mixed atoms Zr and Hf are labeled and give rise to the different configurations possible of the HZO solid solution.

Configurations (polar o-phase)	Position of atoms	Energy (meV)	Multiplicity	Population at T = 723 K (%)
HZO_211_A	Zr-Hf-Zr-Hf-Zr-Hf-Zr-Hf	2.03	4	2.12
HZO_211_B	Zr-Zr-Zr-Hf-Hf-Zr-Hf-Hf	7.73	8	3.88
HZO_211_C	Zr-Hf-Zr-Zr-Hf-Zr-Hf-Hf	7.87	8	3.87
HZO_211_D	Zr-Hf-Zr-Hf-Zr-Zr-Hf-Hf	8.16	8	3.86
HZO_211_E	Hf-Zr-Hf-Zr-Zr-Hf-Zr-Hf	1.80	4	2.13
HZO_211_F	Zr-Zr-Zr-Hf-Hf-Hf-Zr-Hf	7.42	8	3.90
HZO_211_G	Zr-Hf-Zr-Zr-Hf-Hf-Zr-Hf	7.56	8	3.89
HZO_211_H	Hf-Zr-Hf-Zr-Hf-Zr-Hf-Zr	0.93	4	2.16
HZO_211_I	Zr-Zr-Zr-Zr-Hf-Hf-Hf-Hf	0.00	2	1.10
HZO_211_J	Hf-Hf-Zr-Zr-Hf-Hf-Zr-Zr	109.15	2	0.19
HZO_211_K	Zr-Zr-Hf-Hf-Hf-Zr-Hf-Zr	7.76	8	3.88
HZO_211_L	Hf-Zr-Zr-Hf-Zr-Hf-Zr-Hf	9.13	4	1.90
HZO_211_M	Hf-Hf-Zr-Zr-Zr-Zr-Hf-Hf	0.51	2	1.09
HZO_121_A	Hf-Zr-Hf-Zr-Hf-Zr-Hf-Zr	7.65	2	0.97
HZO_121_B	Zr-Zr-Zr-Hf-Zr-Hf-Hf-Hf	6.95	8	3.93
HZO_121_C	Zr-Hf-Zr-Zr-Zr-Hf-Hf-Hf	7.91	8	3.87
HZO_121_D	Zr-Hf-Zr-Hf-Zr-Zr-Hf-Hf	7.755	8	3.88
HZO_121_E	Zr-Hf-Zr-Hf-Zr-Hf-Hf-Zr	8.01	8	3.86
HZO_121_F	Zr-Zr-Zr-Zr-Hf-Hf-Hf-Hf	6.83	2	0.98
HZO_121_G	Zr-Zr-Zr-Hf-Hf-Zr-Hf-Hf	8.09	8	3.86
HZO_121_H	Zr-Zr-Zr-Hf-Hf-Hf-Hf-Zr	7.30	8	3.91
HZO_121_I	Hf-Zr-Hf-Zr-Zr-Hf-Zr-Hf	8.40	2	0.96
HZO_121_J	Hf-Hf-Zr-Zr-Hf-Hf-Zr-Zr	7.56	2	0.97
HZO_121_K	Zr-Zr-Hf-Hf-Zr-Hf-Hf-Zr	7.64	8	3.89
HZO_121_L	Hf-Zr-Zr-Hf-Hf-Zr-Zr-Hf	9.43	2	0.94
HZO_121_M	Hf-Hf-Zr-Zr-Zr-Zr-Hf-Hf	8.01	2	0.96
HZO_121_N	Hf-Zr-Zr-Hf-Zr-Hf-Hf-Zr	6.43	2	0.99
HZO_112_A	Hf-Zr-Zr-Hf-Zr-Hf-Hf-Zr	9.88	4	1.87
HZO_112_B	Hf-Hf-Zr-Hf-Zr-Hf-Zr-Zr	8.61	8	3.83
HZO_112_C	Hf-Zr-Hf-Hf-Zr-Hf-Zr-Zr	7.97	8	3.87
HZO_112_D	Hf-Zr-Zr-Hf-Hf-Hf-Zr-Zr	7.95	8	3.87
HZO_112_E	Hf-Zr-Zr-Hf-Zr-Hf-Zr-Hf	8.39	8	3.845
HZO_112_F	Hf-Hf-Zr-Hf-Zr-Zr-Hf-Zr	7.74	8	3.88
HZO_112_G	Hf-Zr-Zr-Hf-Zr-Zr-Hf-Hf	7.73	8	3.88
HZO_112_H	Zr-Zr-Zr-Zr-Hf-Hf-Hf-Hf	6.83	2	0.98
HZO_112_I	Hf-Hf-Zr-Hf-Hf-Zr-Zr-Zr	7.05	8	3.92
HZO_112_J	Hf-Zr-Zr-Hf-Hf-Zr-Zr-Hf	827.69	4	0.00
HZO_112_K	Hf-Hf-Zr-Zr-Hf-Hf-Zr-Zr	7.56	2	0.97
HZO_112_L	Hf-Hf-Zr-Zr-Zr-Zr-Hf-Hf	8.01	2	0.96

Table S3. Table with a scheme for the position of atoms for each configuration for the polar o-phase, as well as its energy (normalized to the the minimum configuration energy), the configuration's multiplicity and its population (%) at 723 K. The notation 211, 121 and 112 refers to the 3 directions of space in which the crystal structure can exist.

Configurations (t-phase)	Position of atoms	Energy (meV)	Multiplicity	Population at T = 723 K (%)
HZO_122_A	Zr-Zr-Hf-Hf-Zr-Zr-Hf-Hf	0.00	4	1.92
HZO_122_B	Zr-Zr-Zr-Hf-Zr-Hf-Hf-Hf	0.62	16	7.60
HZO_122_C	Zr-Zr-Hf-Hf-Zr-Hf-Zr-Hf	0.72	8	3.79
HZO_122_D	Zr-Zr-Hf-Zr-Zr-Hf-Hf-Hf	0.72	16	7.59
HZO_122_E	Zr-Hf-Zr-Hf-Zr-Hf-Hf-Zr	0.21	8	3.82
HZO_122_F	Zr-Hf-Zr-Hf-Zr-Hf-Zr-Hf	1.63	2	0.93
HZO_122_G	Zr-Hf-Zr-Hf-Zr-Hf-Hf-Zr	1.05	8	3.77
HZO_122_H	Zr-Hf-Hf-Zr-Zr-Hf-Hf-Zr	0.67	4	1.89
HZO_122_I	Zr-Zr-Zr-Zr-Hf-Hf-Hf-Hf	0.82	2	0.94
HZO_122_J	Zr-Hf-Zr-Hf-Hf-Zr-Hf-Zr	1.53	2	0.93
HZO_212_A	Zr-Zr-Hf-Hf-Zr-Zr-Hf-Hf	0.00	4	1.92
HZO_212_B	Zr-Zr-Zr-Hf-Zr-Hf-Hf-Hf	0.70	16	7.59
HZO_212_C	Zr-Zr-Hf-Hf-Zr-Hf-Zr-Hf	0.74	8	3.79
HZO_212_D	Zr-Zr-Hf-Zr-Zr-Hf-Hf-Hf	0.62	16	7.60
HZO_212_E	Zr-Zr-Hf-Hf-Zr-Hf-Hf-Zr	0.19	8	3.82
HZO_212_F	Zr-Hf-Zr-Hf-Zr-Hf-Zr-Hf	1.63	2	0.93
HZO_212_G	Zr-Hf-Zr-Hf-Zr-Hf-Hf-Zr	1.03	8	3.77
HZO_212_H	Zr-Hf-Hf-Zr-Zr-Hf-Hf-Zr	0.67	4	1.89
HZO_212_I	Zr-Zr-Zr-Zr-Hf-Hf-Hf-Hf	0.82	2	0.94
HZO_212_J	Zr-Hf-Zr-Hf-Hf-Zr-Hf-Zr	1.53	2	0.93
HZO_221_A	Zr-Zr-Hf-Hf-Zr-Zr-Hf-Hf	0.00	8	3.84
HZO_221_B	Zr-Zr-Zr-Hf-Zr-Hf-Hf-Hf	0.18	32	15.32
HZO_221_C	Zr-Zr-Hf-Hf-Zr-Hf-Zr-Hf	0.12	8	3.83
HZO_221_D	Zr-Zr-Hf-Hf-Zr-Hf-Hf-Zr	0.08	16	7.67
HZO_221_E	Zr-Hf-Hf-Zr-Zr-Hf-Hf-Zr	0.65	4	1.90
HZO_221_F	Zr-Zr-Zr-Zr-Hf-Hf-Hf-Hf	0.91	2	0.94

Table S4. Table with a scheme for the position of atoms for each configuration for the t-phase, as well as its energy (normalized to the the minimum configuration energy), the configuration's multiplicity and its population (%) at 723 K. The notation 122, 212 and 221 refers to the 3 directions of space in which the crystal structure can exist.

Configurations (m-phase)	Position of atoms	Energy (meV)	Multiplicity	Population at T = 723 K (%)
HZO_112_A	Zr-Hf-Zr-Hf-Zr-Hf-Hf-Zr	1.24	4	1.99
HZO_112_B	Zr-Zr-Zr-Hf-Zr-Hf-Hf-Hf	1.00	8	4.00
HZO_112_C	Zr-Hf-Zr-Zr-Zr-Hf-Hf-Hf	0.80	8	4.01
HZO_112_D	Zr-Hf-Zr-Hf-Zr-Zr-Hf-Hf	9.93	8	3.46
HZO_112_E	Zr-Hf-Zr-Hf-Zr-Hf-Zr-Hf	2.17	4	1.96
HZO_112_F	Zr-Zr-Hf-Hf-Zr-Hf-Hf-Zr	0.79	8	4.01
HZO_112_G	Zr-Hf-Hf-Zr-Zr-Hf-Hf-Zr	0.58	4	2.01
HZO_112_H	Zr-Hf-Hf-Hf-Zr-Zr-Hf-Zr	1.08	8	3.99
HZO_112_I	Zr-Zr-Hf-Hf-Zr-Zr-Hf-Hf	1.92	2	0.98
HZO_112_J	Zr-Zr-Zr-Zr-Hf-Hf-Hf-Hf	0.00	2	1.01
HZO_112_K	Zr-Zr-Zr-Hf-Hf-Hf-Zr-Hf	0.65	8	4.02
HZO_112_L	Zr-Hf-Zr-Hf-Hf-Zr-Zr-Hf	1.30	4	1.99
HZO_112_M	Zr-Zr-Hf-Hf-Hf-Hf-Zr-Zr	0.33	2	1.01
HZO_121_A	Zr-Hf-Hf-Zr-Zr-Hf-Zr-Hf	2.37	4	1.95
HZO_121_B	Zr-Zr-Hf-Zr-Zr-Hf-Hf-Hf	1.26	8	3.98
HZO_121_C	Zr-Hf-Zr-Zr-Zr-Hf-Hf-Hf	1.27	8	3.98
HZO_121_D	Zr-Hf-Hf-Zr-Zr-Zr-Hf-Hf	1.28	8	3.98
HZO_121_E	Zr-Hf-Hf-Zr-Zr-Hf-Hf-Zr	1.88	4	1.97
HZO_121_F	Zr-Zr-Hf-Hf-Zr-Hf-Zr-Hf	1.16	8	3.99
HZO_121_G	Zr-Hf-Zr-Hf-Zr-Hf-Zr-Hf	0.98	4	2.00
HZO_121_H	Zr-Hf-Hf-Hf-Zr-Zr-Zr-Hf	0.82	8	4.01
HZO_121_I	Zr-Zr-Hf-Hf-Zr-Zr-Hf-Hf	1.92	2	0.98
HZO_121_J	Zr-Zr-Zr-Zr-Hf-Hf-Hf-Hf	0.08	2	1.01
HZO_121_K	Zr-Zr-Hf-Zr-Hf-Hf-Hf-Zr	0.19	8	4.05
HZO_121_L	Zr-Hf-Hf-Zr-Hf-Zr-Hf-Zr	0.39	4	2.02
HZO_121_M	Zr-Zr-Hf-Hf-Hf-Hf-Zr-Zr	0.44	2	1.01
HZO_211_A	Zr-Hf-Zr-Hf-Zr-Hf-Zr-Hf	9.78	2	0.86
HZO_211_B	Zr-Zr-Zr-Hf-Zr-Hf-Hf-Hf	9.93	8	3.46
HZO_211_C	Zr-Hf-Zr-Zr-Zr-Hf-Hf-Hf	9.48	8	3.49
HZO_211_D	Zr-Hf-Zr-Hf-Zr-Zr-Hf-Hf	9.48	8	3.49
HZO_211_E	Zr-Hf-Zr-Hf-Zr-Hf-Hf-Zr	9.86	8	3.47
HZO_211_F	Zr-Zr-Hf-Zr-Zr-Hf-Hf-Hf	9.32	8	3.50
HZO_211_G	Zr-Zr-Hf-Hf-Zr-Zr-Hf-Hf	10.13	2	0.86
HZO_211_H	Zr-Zr-Hf-Hf-Zr-Hf-Hf-Zr	10.13	8	3.45
HZO_211_I	Zr-Hf-Hf-Zr-Zr-Hf-Hf-Zr	10.11	2	0.86
HZO_211_J	Zr-Zr-Zr-Zr-Hf-Hf-Hf-Hf	8.33	2	0.88
HZO_211_K	Zr-Zr-Zr-Hf-Hf-Hf-Hf-Zr	9.33	8	3.50
HZO_211_L	Zr-Hf-Zr-Hf-Hf-Zr-Hf-Zr	8.75	2	0.88
HZO_211_M	Zr-Hf-Zr-Hf-Hf-Hf-Zr-Zr	9.47	2	0.87
HZO_211_N	Zr-Hf-Hf-Zr-Hf-Zr-Zr-Hf	11.51	2	0.84

Table S5. Table with a scheme for the position of atoms for each configuration for the m-phase, as well as its energy (normalized to the the minimum configuration energy), the configuration's multiplicity and its population (%) at 723 K. The notation 211, 121 and 112 refers to the 3 directions of space in which the crystal structure can exist.